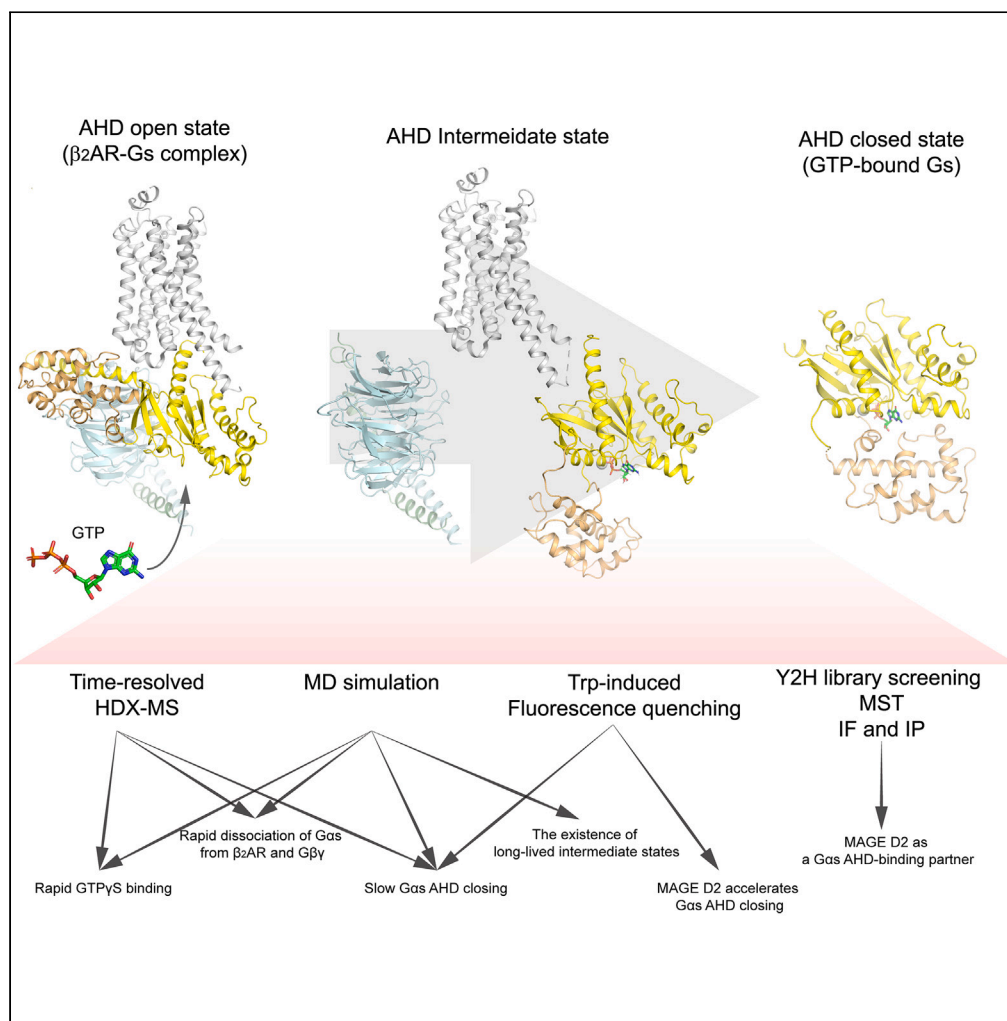


Article

G α s slow conformational transition upon GTP binding and a novel G α s regulator

Donghoon Ahn,
Davide Provasi,
Nguyen Minh Duc,
..., Yang Du, Marta
Filizola, Ka Young
Chung

marta.filizola@mssm.edu
(M.F.)
kychung2@skku.edu (K.Y.C.)

Highlights

The stepwise conformational changes of the β_2 AR-Gs on GTP γ S binding are analyzed

GTP γ S binding rapidly dissociates G α s from β_2 AR and G $\beta\gamma$

G α s AHD is slowly closed after GTP γ S binding, and long-lived intermediate states exist

MAGE D2, a novel G α s AHD-binding protein, facilitates GTP γ S-induced AHD closing

Article

G α s slow conformational transition upon GTP binding and a novel G α s regulator

Donghoon Ahn,^{1,7} Davide Provasi,^{2,7} Nguyen Minh Duc,^{1,7,8} Jun Xu,³ Leslie Salas-Estrada,² Aleksandar Spasic,² Min Woo Yun,¹ Juyeong Kang,^{1,4} Dongmin Gim,^{1,4} Jaecheol Lee,^{1,4,5} Yang Du,⁶ Marta Filizola,^{2,9,*} and Ka Young Chung^{1,9,10,*}

SUMMARY

G proteins are major signaling partners for G protein-coupled receptors (GPCRs). Although stepwise structural changes during GPCR–G protein complex formation and guanosine diphosphate (GDP) release have been reported, no information is available with regard to guanosine triphosphate (GTP) binding. Here, we used a novel Bayesian integrative modeling framework that combines data from hydrogen-deuterium exchange mass spectrometry, tryptophan-induced fluorescence quenching, and metadynamics simulations to derive a kinetic model and atomic-level characterization of stepwise conformational changes incurred by the β_2 -adrenergic receptor (β_2 AR)–Gs complex after GDP release and GTP binding. Our data suggest rapid GTP binding and GTP-induced dissociation of G α s from β_2 AR and G $\beta\gamma$, as opposed to a slow closing of the G α s α -helical domain (AHD). Yeast-two-hybrid screening using G α s AHD as bait identified melanoma-associated antigen D2 (MAGE D2) as a novel AHD-binding protein, which was also shown to accelerate the GTP-induced closing of the G α s AHD.

INTRODUCTION

Heterotrimeric G proteins are a family of guanine nucleotide-binding proteins composed of three distinct subunits (G α , G β , and G γ). G proteins exist in inactive or active states depending on whether the nucleotide bound to G α is guanosine diphosphate (GDP) or guanosine triphosphate (GTP). Specifically, GDP-bound G α forms an inactive trimeric complex with G $\beta\gamma$, whereas GTP-bound G α exists in an active state dissociated from both receptor and G $\beta\gamma$ subunits¹ (Figure 1A).

G protein-coupled receptors (GPCRs), one of the largest groups of cell-surface receptors and validated drug targets,^{2,3} act as guanine nucleotide exchange factors (GEFs) by triggering GDP release from G α on their binding to G proteins (Figure 1A). Given the approximately 10-fold higher concentration of GTP than GDP in the cell,⁴ GTP binding to the empty nucleotide-binding pocket is believed to occur quickly and induce the conformational changes in G α leading to its dissociation from the receptor and G $\beta\gamma$, resulting in the full activation of G α and G $\beta\gamma$ (Figure 1A).

Several high-resolution three-dimensional structures of GPCR–G protein complexes,^{5–18} alongside high-resolution G protein structures bound to GDP or GTP equivalents,^{19–23} have provided an unprecedented level of atomistic detail into GPCR–G protein signaling (see examples in Figures S1A–S1C). These structures have revealed that the nucleotide-binding pocket is located between the Ras-like GTPase domain (RD) and the α -helical domain (AHD) of G α .^{23,24} (Figures 1A and S1A). GPCRs bind to the G α RD, particularly at the α 5 helix and a hydrophobic core formed by the α N– β 1 hinge, β 2– β 3, and α 5, mostly through interactions with their cytosolic core and intracellular loops (ICLs) (Figure S1B).^{25,26} Notably, these interactions have been suggested to trigger allosteric conformational changes near the nucleotide-binding pocket, which lead to GDP release and the opening of the G α AHD with respect to the RD^{24–26} (Figures 1A and S1B). In contrast to the large differences between the GDP-bound and nucleotide-free receptor-bound G α states (compare Figure S1A with Figure S1B), GDP-bound and GTP-bound G α showed very little structural discrepancies, which are mostly limited to Switch II rearrangements at the G $\beta\gamma$ -binding interface (Figure S1C).

¹School of Pharmacy, Sungkyunkwan University, Suwon 16419, Republic of Korea

²Department of Pharmacological Sciences, Icahn School of Medicine at Mount Sinai, New York, NY 10029, USA

³Molecular and Cellular Physiology, School of Medicine, Stanford University, Stanford, CA 94305, USA

⁴Department of Biopharmaceutical Convergence, Sungkyunkwan University, Suwon 16419, Republic of Korea

⁵Biomedical Institute for Convergence at SKKU (BICS), Sungkyunkwan University, Suwon 16419, Republic of Korea

⁶School of Life and Health Sciences, Kobilka Institute of Innovative Drug Discovery, Chinese University of Hong Kong, Shenzhen, Guangdong 518172, China

⁷These authors contributed equally

⁸Present address: Department of Medical Biochemistry and Biophysics, Karolinska Institutet, 17177 Stockholm, Sweden

⁹Senior author

¹⁰Lead contact

*Correspondence: marta.filizola@mssm.edu (M.F.), kychung2@skku.edu (K.Y.C.) <https://doi.org/10.1016/j.isci.2023.106603>



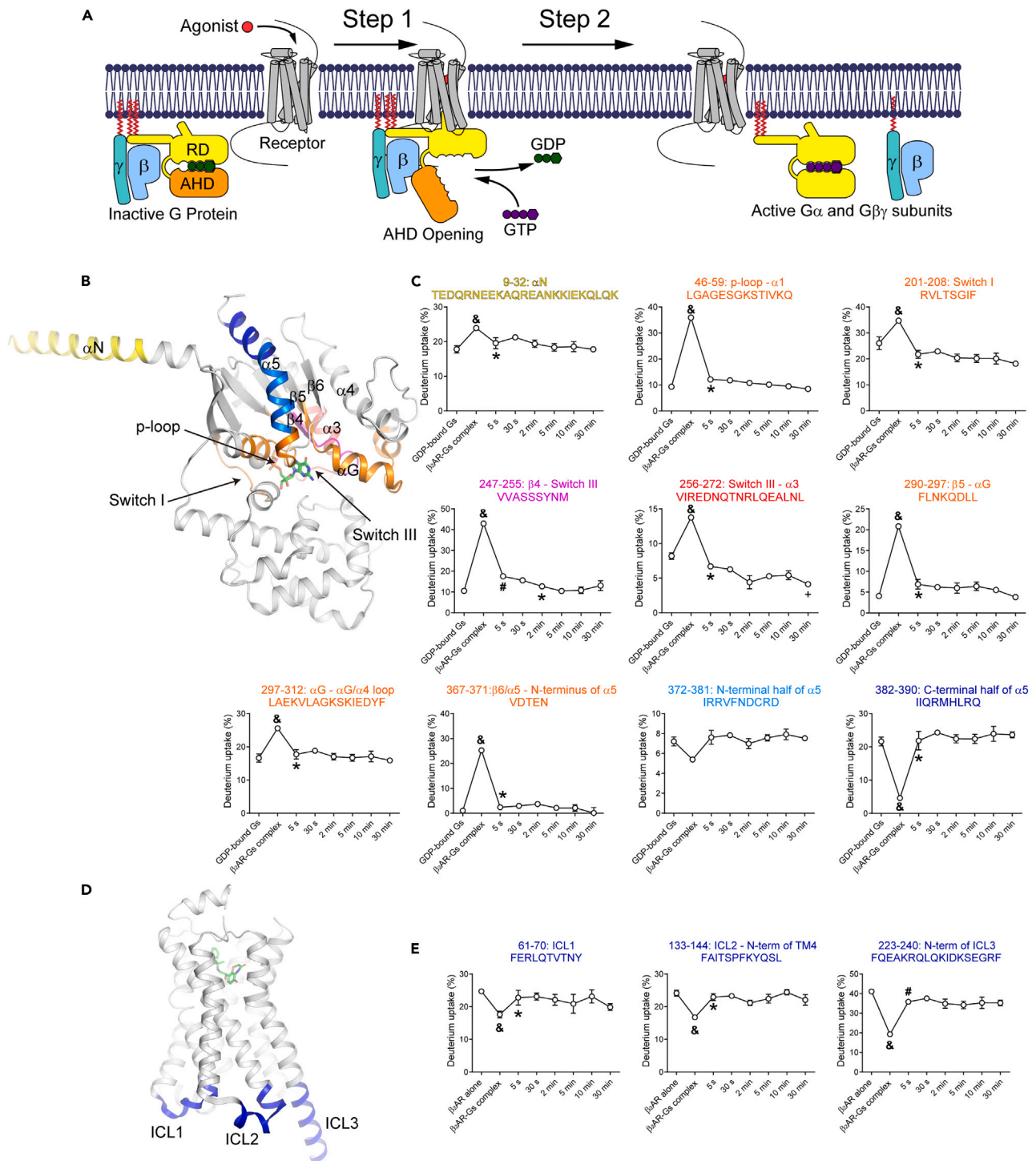


Figure 1. Time-resolved analysis of β_2 AR and $G\alpha_s$ RD after $GTP\gamma S$ addition to the β_2 AR- $G\alpha_s$ complex

(A) G protein activation pathway illustrating the GPCR-mediated GDP release (Step 1), and $GTP\gamma S$ binding-induced GPCR-G protein complex dissociation and G protein activation (Step 2). RD indicates the Ras-like GTPase domain, and AHD indicates the α -helical domain of the $G\alpha$ subunit.

(B) Regions in the $G\alpha_s$ RD showing HDX profile changes after $GTP\gamma S$ addition color-coded on the X-ray crystal structure of GDP-bound G_s heterotrimer (PDB: 6EG8). $G\beta\gamma$ is omitted for clarity.

(C) Pulse-labeling deuterium uptake plots of the peptic peptides color-coded as in (B).

(D) Regions in the β_2 AR showing HDX level changes after $GTP\gamma S$ addition highlighted in blue on the X-ray crystal structure of the β_2 AR- G_s complex (PDB: 3SN6). G_s is omitted for clarity.

Figure 1. Continued

(E) Pulse-labeling deuterium uptake plots of the peptic peptides colored blue as in (D). For (C) and (E), the mass differences >0.3 Da were considered significant. To compare two different time points, a paired t-test was used, and $p < 0.05$ was considered statistically significant. &, the HDX level of the nucleotide-free β_2 AR-Gs complex is significantly different from the HDX levels of GDP-bound Gs or β_2 AR alone. *, the first time point after GTP γ S addition when the HDX level returned to that of the GDP-bound Gs or β_2 AR alone. #, the first time point after GTP γ S addition when the HDX level was significantly different from that of the nucleotide-free β_2 AR-Gs complex but not yet returned to the levels of GDP-bound Gs or β_2 AR alone. +, first time point showing a statistically significant difference from the time point (*). The data represent the average value of three technically independent experiments. Error bars represent the standard error of the mean. Data are plotted using a non-linear/non-logarithmic scale. See also [Figures S1](#) and [S2](#), as well as [Data S1](#).

Notwithstanding the level of molecular detail revealed by these structures, the complete series of time-resolved conformational transitions undergone by $G\alpha$ during its activation process is unclear. Given the importance of these transitions, they have been the focus of extensive research in recent years, using a variety of biophysical, biochemical, and computational approaches.^{9,20,27–33} Notably, both computational³⁴ and experimental²⁷ studies support the existence of alternative transient intermediates to the reported high-resolution structures during receptor-induced GDP release and GPCR-G protein complex formation ([Figure 1A](#), step 1). In particular, our previous experimental study using hydrogen/deuterium exchange mass spectrometry (HDX-MS) in a time-resolved manner (pulse-labeling HDX-MS) revealed the stepwise conformational changes during β_2 -adrenergic receptor (β_2 AR)-Gs complex formation and GDP release, which confirmed that the early β_2 AR-Gs complex adopts a transient conformation that is different from the reported X-ray crystal structure of the nucleotide-free β_2 AR-Gs complex (PDB: 3SN6).²⁷

Here, we used pulse-labeling HDX-MS ([Figure S1D](#)) to investigate the time-resolved conformational changes incurred by β_2 AR and Gs after guanosine 5'-O-[γ -thio]triphosphate (GTP γ S), a non-hydrolyzable GTP analog, was added to the nucleotide-free β_2 AR-Gs complex ([Figure 1A](#), step 2). We further analyzed the movement of the $G\alpha$ s AHD by monitoring its separation from the $G\alpha$ s RD using a tryptophan-induced fluorescence quenching (TrIQ) technique. These data were then integrated with the results of well-tempered metadynamics simulations³⁵ using a novel integrative modeling framework that combines notions of Bayesian inference³⁶ with the Maximum Caliber (MaxCal) principle,^{37,38} Markov State Modeling (MSM),^{39,40} and transition path theory (TPT).⁴¹ The goal was to translate experimental observations of conformational changes incurred by the β_2 AR-Gs complex after GTP γ S addition into structural ensembles of the most probable metastable states sampled by $G\alpha$ s on GTP γ S binding and their kinetic relationships. Finally, we used yeast-two-hybrid (Y2H) library screening to identify $G\alpha$ s AHD-binding proteins that regulate the kinetics during the GTP binding-induced closing of the $G\alpha$ s AHD.

RESULTS**Rapid GTP γ S binding to $G\alpha$ s**

HDX-MS translates measurements of the exchange between amide hydrogens in the protein backbone and deuterium in the solvent in terms of the stability of the protein's secondary structure as well as its solvent accessibility.⁴² Accordingly, HDX-MS can provide conformational information about the receptor-G protein interfaces, nucleotide-binding pocket, and GTP-induced allosteric conformational changes, albeit not at the single-residue or atomic-level resolution. To analyze the stepwise conformational changes incurred by the β_2 AR-Gs complex upon GTP γ S binding, we prepared the nucleotide-free β_2 AR-Gs complex for pulse-labeling HDX-MS experiments, as described in the [STAR Methods \(Figure S1D\)](#). Briefly, we collected aliquots of the agonist-bound β_2 AR, GDP-bound Gs, and nucleotide-free β_2 AR-Gs complex, as well as aliquots of protein samples at specific time points (5 s, 30 s, 2 min, 5 min, 10 min, and 30 min) after GTP γ S addition to the nucleotide-free β_2 AR-Gs complex. The collected samples were immediately exposed to a D_2O pulse for 10 s ([Figure S1D](#)). The detailed HDX-MS analysis parameters and mass spectrum information of all analyzed peptides are summarized in [Data S1](#).

The HDX levels were higher for peptides near the nucleotide-binding pocket of $G\alpha$ s (P loop through $\alpha 1$, Switch I, Switch III, $\beta 5$ through the $\alpha G/\alpha 4$ loop, and the $\beta 6/\alpha 5$ loop through the N-terminus of $\alpha 5$) in the nucleotide-free β_2 AR-Gs complex compared with those of GDP-bound Gs ([Figure 1B](#), magenta-, red-, and orange-colored regions; [Figure 1C](#), compare the first two time points in plots of peptides 46–59, 201–208, 247–255, 256–272, 290–297, 297–312, and 367–371), reflecting increased solvent accessibility and structural dynamics after GDP release, which is consistent with our previous reports.^{27,43,44}

Within 5 s of adding GTP γ S to the nucleotide-free β_2 AR-Gs complex, the HDX levels of all these peptides, except for peptide 247–255 ($\beta 4$ through Switch III), returned to the HDX levels of the GDP-bound Gs,

whereas the HDX levels of peptide 247–255 returned to approximately 80–90% of the HDX levels of GDP-bound Gs (Figure 1C), suggesting rapid binding of GTP γ S at the nucleotide-binding pocket. Although the HDX levels of peptides 46–59, 201–208, 290–297, 297–312, and 367–371 of G α s did not change significantly after 5 s (Figure 1C; orange-colored regions in Figure 1B), the HDX levels of peptide 256–272 (Switch III through α 3) continued to change during 30 min, becoming significantly lower than those of GDP-bound Gs at the end of the experiment (Figure 1C; red-colored region in Figure 1B). Similarly, the HDX levels of peptide 247–255 (β 4 through Switch III) continued to decrease after their drastic change within 5 s, but for only 2 min, ultimately returning to the levels of the GDP-bound Gs (Figure 1C; magenta-colored region in Figure 1B). In summary, the pulse-labeling HDX-MS data collected for peptides near the nucleotide-binding pocket suggested rapid GTP γ S binding (within 5 s) and additional prolonged conformational changes at Switch III after GTP γ S binding.

Rapid dissociation of G α s from β_2 AR and G $\beta\gamma$ after GTP γ S binding

The HDX levels were lower at the β_2 AR–Gs interface (C-terminal half of α 5 of G α s and ICLs 1, 2, and 3 of β_2 AR) in the nucleotide-free β_2 AR–Gs complex compared to the GDP-bound Gs (Figure 1B, blue-colored regions; Figure 1C, compare the first two time points in the plot of peptide 382–390), as well as compared with the levels of the agonist-bound β_2 AR alone (Figure 1D, blue-colored regions; Figure 1E, compare the first two time points in all plots). This suggested reduced solvent accessibility and stabilization of the secondary structures at the β_2 AR–Gs interface, which is consistent with our previous reports.^{27,43,44} The HDX levels of the peptide corresponding to the N-terminal half of α 5 also showed a similar trend, although the differences were small and not significant (less than 0.3 Da) (Figure 1B, light blue-colored region; Figure 1C, peptide 372–381). The HDX levels of α N were higher in the β_2 AR–Gs complex compared with those detected in the GDP-bound Gs (Figure 1B, yellow-colored region; Figure 1C, compare the first two time points in the plot of peptide 9–32), suggesting that α N undergoes conformational changes on β_2 AR–Gs complex formation. Within 5 s of GTP γ S addition, the HDX levels of these regions returned to those of GDP-bound Gs (Figure 1C, peptides 9–32 and 382–390) or the agonist-bound β_2 AR alone (Figure 1E), suggesting that GTP γ S-bound G α s dissociates rapidly from the receptor.

Pulse-labeling HDX-MS analysis of G $\beta\gamma$ revealed rapid conformational changes in G β at α N/WD1 S1 loop, WD1 S3 through S4, and WD2 S2 after GTP γ S addition (Figure S2). The HDX levels of G β α N/WD1 S1 loop were higher in the nucleotide-free β_2 AR–Gs complex than those of GDP-bound Gs and quickly (within 5 s) returned to the level of the GDP-bound Gs after GTP γ S addition (Figure S2, orange-colored region, peptide 33–46). The HDX levels of G β WD1 S3 through S4 and those of WD2 S2 did not differ between GDP-bound Gs and the nucleotide-free β_2 AR–Gs complex (Figure S2, cyan-colored regions, compare the first two time points in plots of peptides 81–99 and 111–118); however, on GTP γ S addition to the β_2 AR–Gs complex, these regions showed increased HDX levels within only 5 s, which plateaued after 30 s (Figure S2, cyan-colored regions, peptides 81–99 and 111–118). These HDX level changes in peptides 81–99 and 111–118 of G $\beta\gamma$ likely reflect conformational changes because of the dissociation of G $\beta\gamma$ from G α s, given that they were observed only after GTP γ S addition but not on β_2 AR–Gs complex formation. Overall, these results suggest that G $\beta\gamma$ may also quickly dissociate from GTP γ S-bound G α s.

Slow conformational changes of the G α s AHD after GTP γ S binding

A notable observation of the pulse-labeling HDX-MS analysis was that several G α s AHD peptides showed slow changes in the HDX levels on GTP γ S binding. The HDX levels of these peptides were higher in the nucleotide-free β_2 AR–Gs complex compared with those in GDP-bound Gs (Figure 2A, compare the first two time points in all plots), reflecting the AHD displacement and increased local conformational dynamics in the nucleotide-free β_2 AR–Gs complex compared to the GDP-bound Gs (compare Figures S1A and S1B).

Except for peptide 178–193 (α E through the α E/ α F loop), whose HDX levels quickly returned to those of the GDP-bound Gs within 5 s of GTP γ S addition (Figure 2A, orange-colored region), the HDX levels of other peptides depicted in Figure 2A showed slow and continued changes (peptides 108–118, 119–126, 126–132, and 190–197). Peptides 108–118 (C-terminus of α A through the α A/ α B loop) and 126–132 (α B) slowly returned to the HDX levels of GDP-bound Gs within 30 min (Figure 2A, green-colored region). Peptides 119–126 (α A/ α B loop through α B) and 190–197 (α E/ α F loop through α F) returned to the HDX levels of GDP-bound Gs after 2–5 min (Figure 2A, dark green-colored regions). These results suggested that the G α s AHD undergoes relatively slow and continued conformational changes even after GTP γ S binding to

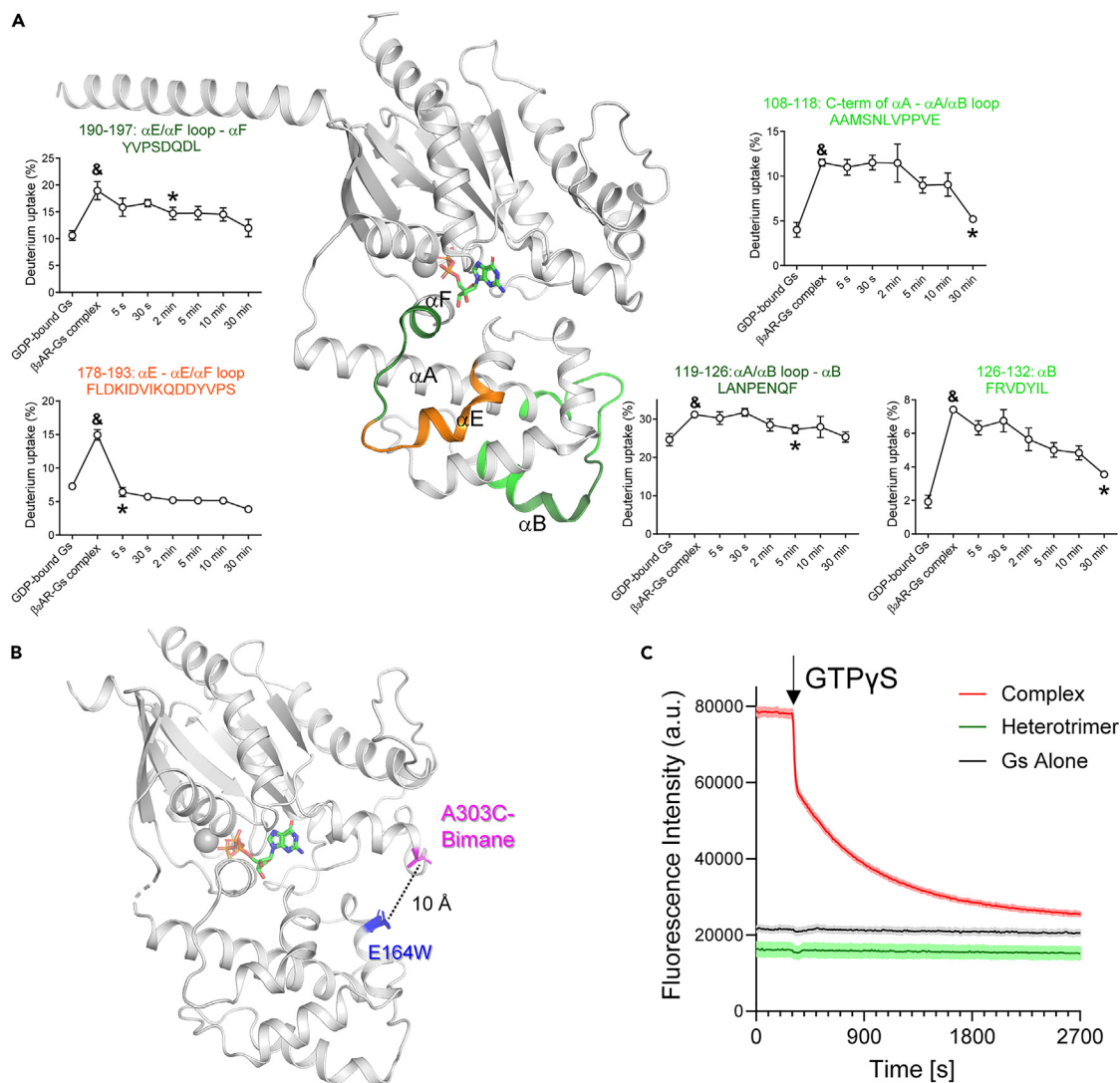


Figure 2. Time-resolved analysis of conformational changes of the $G\alpha_s$ AHD after $GTP\gamma S$ addition to the $\beta_2AR-G\alpha_s$ complex

(A) Regions in the $G\alpha_s$ AHD showing HDX level changes after $GTP\gamma S$ addition color-coded on the X-ray crystal structure of the GDP-bound Gs heterotrimer (PDB: 6EG8). $G\beta\gamma$ is omitted for clarity. Pulse-labeling deuterium uptake plots are shown for the color-coded peptic peptides. The mass differences >0.3 Da were considered significant. To compare two different time points, a paired t-test was used, and $p < 0.05$ was considered statistically significant. &, the HDX level of the nucleotide-free β_2AR-Gs complex is significantly different from that of GDP-bound Gs. *, the first time point after $GTP\gamma S$ addition when the HDX level returned to that of the GDP-bound Gs. The data represent the average value of three technically independent experiments. Error bars represent the standard error of the mean. Data are plotted using a non-linear/non-logarithmic scale.

(B) Residues labeled with bimane (magenta) or mutated to Trp (blue) indicated as sticks on the X-ray crystal structure of $GTP\gamma S$ -bound $G\alpha_s$ (PDB: 1A2T). (C) Time-resolved tryptophan-induced bimane quenching analysis of the β_2AR-Gs complex after $GTP\gamma S$ addition. The data are mean of three independently labeled experiments and error bars represent the standard error of the mean. See also Figures S1–S3, as well as Data S1.

$G\alpha_s$ and its consequent dissociation from the receptor and $G\beta\gamma$ (within 5 s in the current experimental system, as shown in Figures 1B–1E).

Slow AHD closing kinetics after $GTP\gamma S$ binding

To understand whether the slow HDX changes in the $G\alpha_s$ AHD (Figure 2A) are related to the slow AHD closing kinetics, we developed an experimental system that monitors the separation between the RD and AHD using TrIQ (Figure 2B). The bimane fluorescence is quenched when aromatic residues such as Trp, Tyr, and Phe are nearby.⁴⁵ Therefore, given their vicinity (α -carbon atoms within 10 Å) in the $GTP\gamma S$ -bound $G\alpha_s$ crystal structure (PDB: 1A2T), we engineered $G\alpha_s$ to replace residue A303 in the RD with Cys for

monobromobimane labeling and residue E164 in the AHD with Trp (Figure 2B). In this construct, the bimane fluorescence is expected to be quenched in the nucleotide-bound closed conformation of $G\alpha s$ (see Figures S1A–S1C) but unquenched in the nucleotide-free open conformation (see Figure S1B). As there are other Cys residues in $G\alpha s$, we mutated all solvent-exposed Cys residues (Figure S3A, red-colored residues) to Ser to prevent unwanted bimane labeling, and confirmed that these mutations do not affect the function of $G\alpha s$ by measuring successful BODIPY-FL-GTP γ S uptake profiles (Figure S3B) and heterotrimer formation with $G\beta\gamma$ (Figure S3C).

We first verified the suitability of this construct for monitoring the separation between the RD and AHD by recording (a) similar bimane fluorescence values between GDP-bound and GTP γ S-bound $G\alpha s$ (Figure S3D), in line with their conformational states being closed (Figure S1C); and (b) higher bimane fluorescence values for the nucleotide-free β_2AR –Gs complex compared to the GDP-bound Gs heterotrimer or GDP-bound $G\alpha s$ (Figure S3E), in line with AHD being displaced in the nucleotide-free β_2AR –Gs complex (Figure S1B).

We then used this TrIQ method to monitor $G\alpha s$ AHD closing in a time-resolved manner. After GTP γ S addition to the nucleotide-free β_2AR –Gs complex, the bimane fluorescence decreased in two steps: an initial fast decrease (with a time constant of 50 ± 8 s), followed by a slow (time constant of 655 ± 10 s) and continued decrease (Figure 2C). This observation suggested that the AHD may adopt long-lived intermediate conformational states during its GTP γ S binding-induced closing.

Simulated conformational states of $G\alpha s$ after GDP release and GTP binding

To obtain an atomic-level characterization of $G\alpha s$ conformations after GDP release and GTP binding (Figure 1A, step 2), we simulated $G\alpha s$ either starting from its closed, GTP γ S-bound crystal structure (PDB: 1AZT²²) in the presence of a bound Mg^{2+} ion and a water environment or starting from its nucleotide-free conformation in the β_2AR –Gs complex (PDB: 3SN6¹⁶) in a hydrated 1-palmitoyl-2-oleoyl-*sn*-glycero-3-phosphocholine (POPC)/10% cholesterol lipid bilayer (see the STAR Methods for details of the simulated systems). In agreement with the most favorable coordination state of Mg^{2+} observed in the structures of GTPases,⁴⁶ the ion in the GTP γ S-bound $G\alpha s$ system remained coordinated, on average, by 6 residues (identified by the number of heavy atoms within 2.5 Å from the ion) for more than 90% of simulation time and was coordinated by 5 residues and a water molecule for the remainder of the simulations. Because standard molecular dynamics (MD) simulations would require very long simulation times to reproduce the large conformational changes between the closed and open states of $G\alpha s$, after equilibration of the GTP γ S– $G\alpha s$ and β_2AR –Gs systems, we used well-tempered metadynamics³⁵ to enhance the sampling of the separation and relative orientation between their RD and AHD regions using the two collective variables (CVs) illustrated in Figure S5A (see the STAR Methods for simulation details).

The reconstructed free-energy surfaces from simulations are illustrated in Figure S5B. Both the GTP γ S– $G\alpha s$ and nucleotide-free β_2AR –Gs systems explored a wide range of relative orientations of the RD and AHD, with different degrees of separation between the two domains. The GTP γ S– $G\alpha s$ system explored two main conformational ensembles: one encompassing closed AHD states ($CV1 \sim 30^\circ$, $CV2 \leq 2$) and one characterized by open AHD states with large values of the contact map distance ($CV2 \geq 10$), as well as a wide range of angles ($60^\circ \leq CV1 \leq 200^\circ$). The two ensembles exhibited similar free energy but were separated by a free-energy barrier above 10 kT (Figure S5B). Notably, despite the separation between the RD and AHD, and in agreement with previous computational studies,^{31,34} GTP γ S remained firmly bound to the protein throughout the simulation, suggesting that the $G\alpha s$ AHD can exist in the open state even when GTP γ S is bound to $G\alpha s$. The missing lipid-anchored regions in the simulated nucleotide-free β_2AR –Gs model did not result in the detachment of the G protein subunits from the membrane during simulation. The first modeled residue of the $G\alpha$ α N-helix (T9) remained at an average distance of 11.5 Å (8.14 Å, 15.7 Å) from the membrane, whereas the last modeled residue of $G\gamma$ (R62) maintained an average distance of 3.92 Å (3.71 Å, 5.11 Å) from the membrane. Other endpoints of missing segments also remained far from the sampled protein region during simulation, with the $G\alpha$ AHD maintaining average minimum distances of 19.3 Å (with 25th/75th percentiles of 18.4 Å, and 20.6 Å, respectively) from the receptor intracellular loop 3 endpoints, 20.3 Å (19.3 Å, 21.5 Å) from the last modeled residue C341 of the receptor C-terminus, 17.2 Å (6.94 Å, 26.0 Å) from the $G\gamma$ N-terminus, 36.0 Å (34.3 Å, 37.7 Å) from the $G\gamma$ C-terminus, and 38.6 Å (31.5 Å, 48.3 Å) from the $G\alpha$ N-terminus.

In simulations of the nucleotide-free β_2 AR-Gs system, the presence of the receptor and G $\beta\gamma$ appeared to stabilize an ensemble of G α s states with similar degrees of RD-AHD separation to the one observed in the GTP γ S-G α s system. However, it showed more heterogeneous distributions of inter-domain contacts compared with those of the GTP γ S-bound G α s closed state crystal structure (PDB: 1AZT) ($CV1 \sim 30^\circ$; $2 \leq CV2 \leq 10$) or the open state sampled by the GTP γ S-bound G α s system ($60^\circ \leq CV1 \leq 200^\circ$; $7 \leq CV2 \leq 15$). In the absence of GTP γ S, the ensemble of G α s open states ($CV1 > 60^\circ$) was energetically preferred over that of the G α s closed states, with a free-energy difference of 1.28 kT in the case of the nucleotide-free β_2 AR-Gs system and ~ 0 kT in the GTP γ S-bound G α s system (Figure S5B).

Atomic-level kinetic model of G α s activation

Although the metadynamics simulations offered insight into the conformational states that are preferably adopted by G α s in its nucleotide-free form within the β_2 AR-Gs complex or GTP γ S-G α s, the long time-scales needed for nucleotide binding and unbinding, as well as the bias introduced by the metadynamics simulations, limit the type of information that can be directly extracted by such analyses. To obtain an atomic-level description of G α s activation steps after GDP release and GTP binding (Figure 1A, step 2) consistent with the time-resolved conformational changes of the G α s backbone at the second-to-minute timescale from the pulse-labeling HDX-MS (see STAR Methods and Figures 1C and 2A), as well as the G α s conformational states inferred by TrIQ at time zero and infinite (equilibrium) (Figure 2C), we integrated these data with predictions of average residue protection factors and fluorescence quenching computed for each conformational cluster derived from the well-tempered metadynamics simulations³⁵ of the GTP γ S-bound G α s and nucleotide-free β_2 AR-Gs systems.

Specifically, we developed a novel integrative modeling framework that combines the notions of Bayesian inference,³⁶ the MaxCal principle,^{37,38} MSM,^{39,40} and TPT.⁴¹ Accordingly, the experimental and computational data were integrated by deriving a Markov transition matrix of the probabilities of moving from one metadynamics-derived conformational cluster to another. Specifically, the posterior probability of the proposed kinetic model M was expressed as the posterior distribution $p(M|O) \propto p(O|M)p(M)$, where $p(O|M)$ is the likelihood that model M would predict the observed experimental data O and $p(M)$ is the prior probability of the model before observing O , in which the probability of the transition matrix is assigned by MaxCal^{37,38} whereas priors of the equilibrium probabilities correspond to the metadynamics-derived free energies (see STAR Methods for details). TPT analysis of the transition matrix was then used to provide estimates for the mean first passage times of the transitions between the conformational ensembles of G α s bound to GTP γ S or within the nucleotide-free β_2 AR-Gs complex derived from the metadynamics simulations and re-weighted by the experimental data.

In addition to the TrIQ data displayed in Figure 2C, the deuterium uptake fractions of the 15 protein regions spanning the RD and AHD of G α s illustrated in Figures 1C and 2A were used as the observable data O in the aforementioned integrative modeling approach. An established approach that enables estimating HDX protection factors for a given protein conformation⁴⁷ was used to link the HDX-MS experimental data to the conformations of the GTP γ S-G α s and nucleotide-free β_2 AR-Gs systems sampled by metadynamics simulations. After k-means clustering of the metadynamics trajectories using pairwise distances between every third C α atom in G α s projected onto the first 10 time-structure independent component analysis (tICA) components, a set of 16 conformational macrostates, R_s (see STAR Methods for details), was used to compute average residue protection factor estimates for each of the 15 protein regions illustrated in Figures 1C and 2A using 10 frames of each conformational cluster (see STAR Methods). Similarly, these cluster conformations were used to predict fluorescence quenching using a simple contact model.⁴⁵

The proposed Bayesian integrative modeling framework indicated that very good agreement could be achieved between predicted and measured values of the deuterium uptake and fluorescence quenching for 13 out of 15 regions (Figure S6), with peptides 9–32 and 247–255 showing the worst agreement. Only values of the 13 peptides with the best agreement between predicted and experimental measurements were used as observable data for the kinetic model described below.

Figure 3A illustrates the proposed kinetic model of G α s activation on GTP γ S binding, with nodes of the network representing highly populated states (i.e., states whose maximum probability over time is larger than 10%; see values in Table S1) at either time zero or equilibrium (gray and black circles, respectively, in Figure 3A), and the connections among them indicating the timescales needed to transition from one

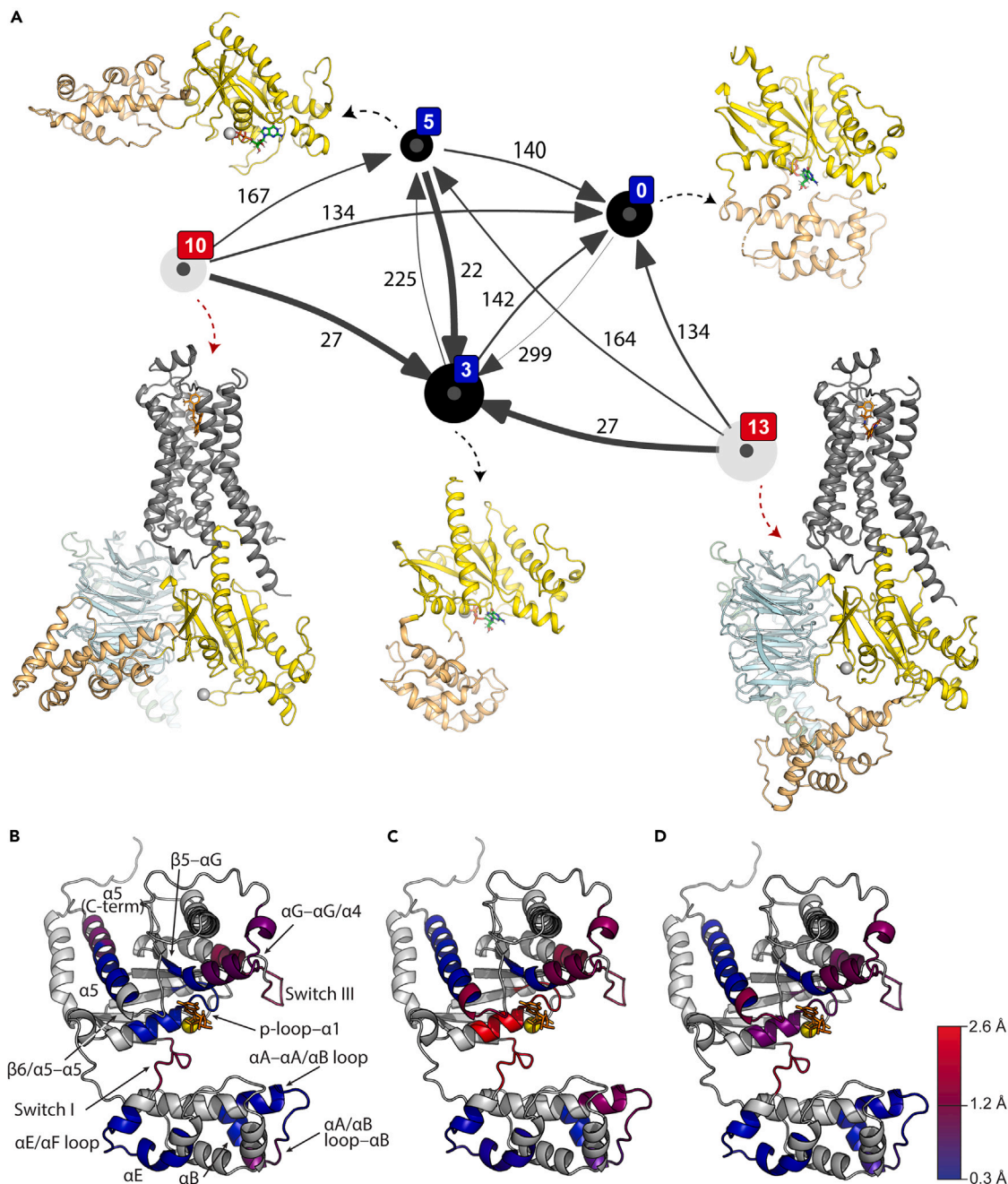


Figure 3. Highly probable conformational states explored by $G\alpha_s$ after $GTP\gamma S$ addition according to the proposed kinetic model

(A) Highly populated states (maximum probability >10%) in the $GTP\gamma S$ - $G\alpha_s$ simulation are indicated by blue numbers, while states in the nucleotide-free β_2AR - G_s simulation are indicated by red numbers. The size of black and gray circles is proportional to the probability of a certain state to be populated at equilibrium (long time scales) or time zero, respectively. Arrows represent mean transition timescales between states, with thick and thin arrows indicating fast and slow transition times, respectively. Mean first passage times (MFPT, in seconds) are reported on the arrows, and their credible intervals are reported in Table S2. Representative structures of each highly populated state are shown in cartoon representations with the receptor in gray, RD of $G\alpha$ in yellow, AHD of $G\alpha$ in light orange, $G\beta$ in light blue, and $G\gamma$ in light green. Magnesium ion (Mg^{2+}) is indicated with a gray sphere, and, where present, $GTP\gamma S$ is shown as sticks.

(B–D) Comparison of the RMSD values of the HDX-MS peptic peptides between macrostates 3 and 0 (B), 3 and 13 (C), and 3 and 10 (D), respectively, color-coded from low (blue) to high (red) values on a representative structure of state 3. See also Figures S4–S7, as well as Tables S1–S3.

state to another. Initially ($t = 0$), $G_{\alpha s}$ mostly explored two nucleotide-free conformational states when bound to β_2AR and $G\beta\gamma$, herein labeled states 10 and 13 with a probability of 29% and 54%, respectively (Table S1), which are characterized by different degrees of separation between the RD and AHD (mean distance of 65.1 Å or 49.4 Å between A303 and E164, respectively) (Figure 3A). This is consistent with the observation that the AHD in the nucleotide-free β_2AR -Gs complex is mobile rather than assuming a fixed position.²⁹

In the presence of GTP γ S, protein states 10 and 13 most rapidly (mean first passage times (MFPTs) of ~ 30 s; see Table S2) transitioned to a highly populated (equilibrium probability of 51%) GTP γ S-bound conformation with an open AHD (state 3, with an inter-domain mean A303–E164 distance of 28.7 Å) (Figure 3A, thick arrows starting from state 10 or 13 to state 3). Slower transitions were recorded from states 10 and 13 to a lower-probability open GTP γ S-bound conformation state 5 (equilibrium probability of 13% and inter-domain mean A303–E164 distance of 77.3 Å; reached, on average, in ~ 160 s) or to a closed conformational state 0 (equilibrium probability of 29% and an inter-domain mean A303–E164 distance of 9.8 Å; reached, on average, in ~ 130 s) (Figure 3A, thin arrows starting from state 10 or 13 to state 5 or 0; and Tables S1 and S2). State 0 closely resembled the X-ray crystal structure of GTP γ S-bound $G_{\alpha s}$ that was used as a starting point for simulations (RMSD of 1.22 Å from PDB: 1AZT).

The half-life of state 3 between the nucleotide-free $G_{\alpha s}$ conformation bound to both β_2AR and $G\beta\gamma$ and the closed GTP γ S-bound conformational state of $G_{\alpha s}$ was estimated to be 142 s, which is shorter than the half-life of the closed GTP γ S-bound conformational state (state 0; 299 s), but much longer than the half-life of the alternative open GTP γ S-bound state (state 5; 22 s) (Figure 3A). Notably, state 5 rapidly converted into state 3 (22 s), but it took much longer for the AHD to transition from state 3 to state 5 (225 s) (Figure 3A). The mean distance between RD A303 and AHD E164 in state 3 (28.7 Å) was smaller than that found in states 10, 13, or 5 (65.1 Å, 49.4 Å, and 77.2 Å, respectively) but larger than that of state 0 (9.8 Å). These results suggest that state 3 may represent the long-lived intermediate state inferred by the data shown in Figure 2C.

Notably, state 3 differed from the X-ray crystal structure of GTP γ S-bound $G_{\alpha s}$, as well as the two most populated states (10 and 13) of the nucleotide-free $G_{\alpha s}$ conformation bound to the β_2AR and $G\beta\gamma$, not only in terms of mean distance separation between RD A303 and AHD E164 but also for the relative orientation between these two domains. RMSD comparison between the identified highly populated long-lived intermediate state 3 of GTP γ S-bound $G_{\alpha s}$ with the identified closest states to the GTP γ S-bound crystal structure 1AZT (state 0) or with the highly probable nucleotide-free $G_{\alpha s}$ conformations bound to the β_2AR and $G\beta\gamma$ (states 10 and 13) revealed specific regions that are, on average, more different than others (Table S3 and Figures 3B–3D). However, in general, the differences were larger between states 3 and 10 or 13 (Figures 3C and 3D) than between states 3 and 0 (Figure 3B). Specifically, regions 46–59 (p-loop- $\alpha 1$), 201–208 (Switch I), and 256–272 (Switch III) exhibited the largest differences between states 3 and 13 (Figure 3C), with Switch I also differing the most between states 3 and 10 (Figure 3D). Although the largest differences (RMSD >2.0) were found between states 3 and 13, pertaining to p-loop- $\alpha 1$, Switch I, and Switch III, the latter two also deviated significantly (RMSD >1.5) in state 3 compared to states 10 and 0.

Novel $G_{\alpha s}$ AHD-binding protein facilitating AHD closing

The G protein signaling cycle is regulated by several proteins, including GEFs (e.g., GPCRs, GIV/Girdin, or Ric-8A) and GTPase-activating proteins [GAPs; e.g., regulators of G protein signaling (RGS)].^{48–52} As our data support slow AHD closing enabled by the long-lived intermediate state of $G_{\alpha s}$ after GTP γ S binding, we searched for an AHD-binding protein that might regulate the AHD closing kinetics. To this end, we employed Y2H library screening with the $G_{\alpha s}$ AHD as bait and identified melanoma-associated antigen D2 (MAGE D2, NM_014599) as a novel $G_{\alpha s}$ AHD-binding protein (Figure S8A).

Mutations in MAGE D2 have been reported to cause Bartter's syndrome, a rare autosomal recessive renal tubular disorder.⁵³ In the same study, MAGE D2 was discovered to interact directly with $G_{\alpha s}$, and other studies suggested that MAGE D2 modulates GPCR signaling.^{53–55}

In this study, we identified that $G_{\alpha s}$ AHD is the binding site of MAGE D2. The overexpressed FLAG-tagged $G_{\alpha s}$ AHD was co-localized with endogenously expressing MAGE D2 in HEK293T cells (Figure 4A). Moreover, turboGFP-tagged MAGE D2 was co-immunoprecipitated with FLAG-tagged $G_{\alpha s}$ AHD in HEK293T cells (Figure 4B). These results suggest that $G_{\alpha s}$ AHD can interact with MAGE D2 in the cellular context.

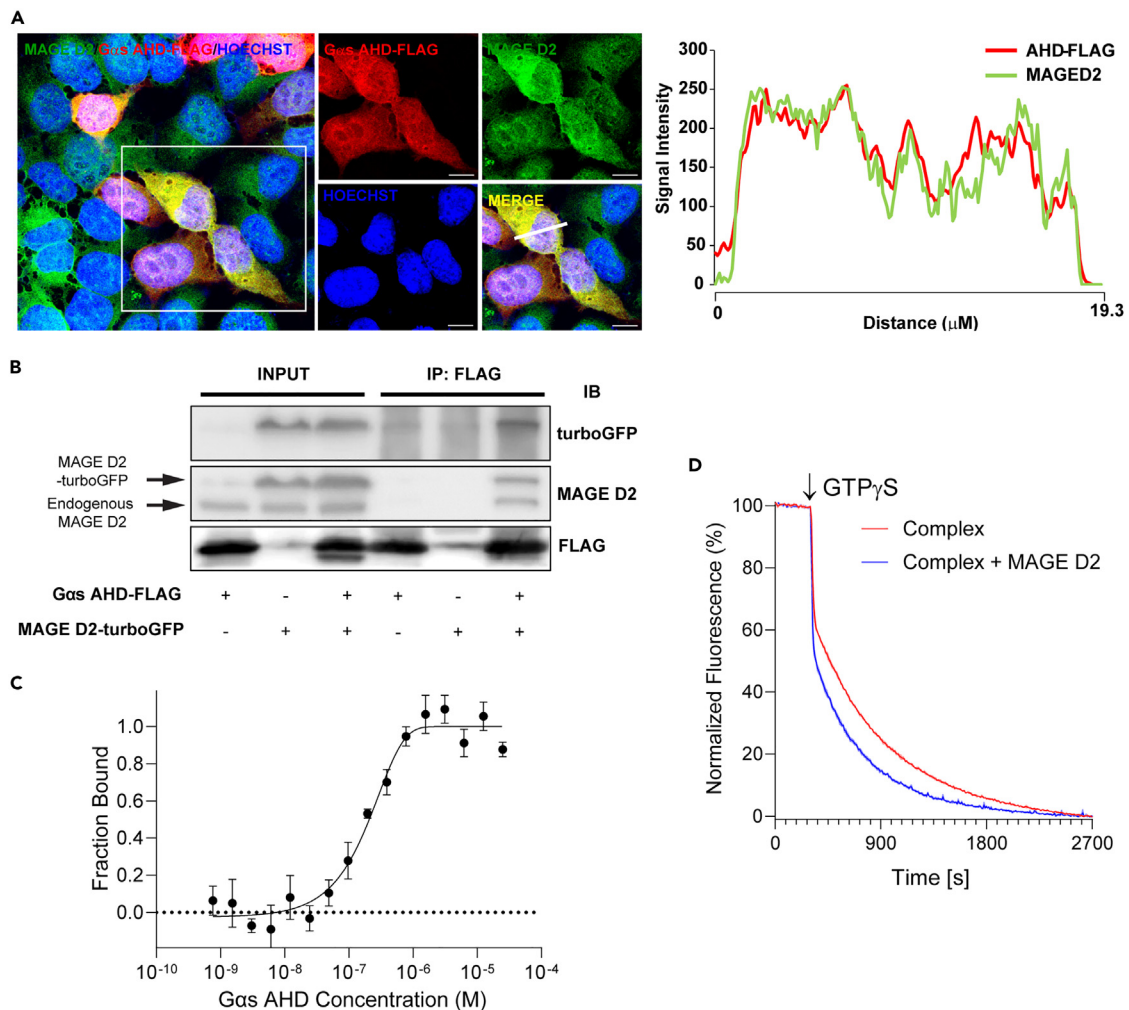


Figure 4. Novel *Gαs* AHD-binding protein that facilitates AHD closing

(A) Representative confocal images of HEK293T cells transiently expressing *Gαs* AHD-FLAG. HEK293T cells were stained with antibodies against FLAG (red) and MAGE D2 (green). Blue represents Hoechst 33342. Right: Representative co-localization tracer profile along the line indicated in the inset. Scale bar, 10 μm.

(B) Immunoblot (IB) analysis of FLAG immunoprecipitates (IP line) and cell lysates (Input line) from HEK293T cells transiently co-expressing *Gαs* AHD-FLAG and MAGE D2-turboGFP.

(C) Binding curve of the *Gαs* AHD with the MAGE D2 MHD analyzed by microscale thermophoresis (MST). A titration series of the *Gαs* AHD was performed, whereas the concentration of fluorescence-labeled MAGE D2 MHD was fixed (see STAR Methods for details). Error bars represent the standard error of the mean of more than three independent experiments.

(D) Time-resolved tryptophan-induced bimane quenching analysis of the β₂AR-Gs complex with or without the MAGE D2 MHD after GTPγS addition. The data are mean of the normalized fluorescence value of three independently labeled experiments and error bars represent the standard error of the mean. See also Figures S3, S8, and S9.

The direct interaction between MAGE D2 and *Gαs* AHD was confirmed using purified proteins and microscale thermophoresis (MST) analysis (Figure 4C). Because all MAGE proteins have a conserved domain called the MAGE homology domain (MHD) that consists of two winged-helix motifs (WH-A and WH-B), which is reported as a protein-protein interaction site,^{56,57} we generated a truncated MAGE D2 construct that only contains the MHD to facilitate protein purification (Figure S8B). MST analysis showed that the purified *Gαs* AHD interacts with purified MAGE D2 MHD with a K_D of 155 ± 47 nM.

We then tested if MAGE D2 binding affects the AHD closing kinetics using the TriQ technique illustrated in Figure 2B. GTPγS was added to the nucleotide-free β₂AR-Gs complex with or without co-incubation of MAGE D2 MHD, and the bimane fluorescence at residue A303C was monitored. Co-incubation of

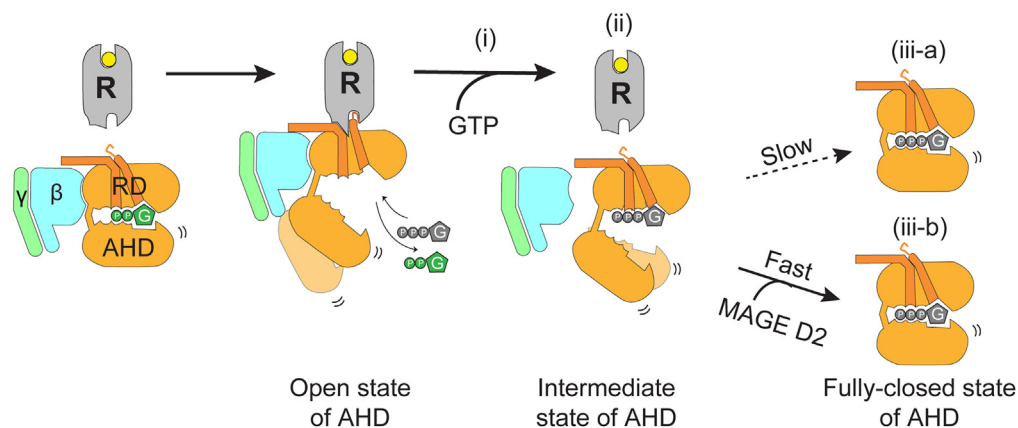


Figure 5. Summary cartoon illustrating the proposed sequence of events after GTP binding to a GPCR-Gs complex with or without MAGE D2

An agonist-activated receptor (R) induces GDP release from Gs, and GTP quickly binds to the empty nucleotide-binding pocket (step i). Upon binding of GTP, G α s rapidly dissociates from the receptor and G $\beta\gamma$ (step ii). The AHD adopts a long-lived intermediate state until it is fully closed, a process that occurs slowly (step iii-a). Closing of the AHD is accelerated in the presence of MAGE D2 (step iii-b). RD indicates the Ras-like GTPase domain, and AHD indicates the α -helical domain.

MAGE D2 MHD accelerated the decrease of bimane fluorescence, suggesting that binding MAGE D2 accelerates the closing of the G α s AHD (Figure 4D).

DISCUSSION

This study describes the sequential conformational transitions incurred by a GPCR-Gs protein complex on GTP γ S binding, using the β_2 AR-Gs complex as a model system. Importantly, we provide the first atomic-level structural interpretation of the stepwise conformational changes the β_2 AR-Gs complex experiences after GDP release and GTP γ S binding, using a novel Bayesian integrative modeling framework that combines experimental observations of GTP γ S-induced β_2 AR-Gs complex dissociation and closing of the G α s AHD from HDX-MS and TriQ data with structural ensembles of β_2 AR-Gs and G α s sampled by metadynamics. Taken together, our data suggest (1) rapid GTP γ S binding to the G α s nucleotide-binding pocket (Figure 5, step 1), (2) rapid G α s dissociation from the receptor and G $\beta\gamma$ (Figure 5, step 2), and (3) slow closing of the G α s AHD and the existence of a long-lived intermediate state (Figure 5, step iii-a). Although we expect that other GPCR-G protein systems will also undergo sequential conformational changes, GPCRs have multi-dimensional signaling profiles that involve different G protein subtypes, which can lead to varying signal intensities and activation kinetics.

Our proposed kinetic model identified highly populated conformational ensembles of both the GTP γ S-bound G α s and the nucleotide-free G α s in complex with β_2 AR and G $\beta\gamma$, with alternative orientations and separations of the AHD with respect to the RD compared with those observed in available high-resolution crystal structures. Moreover, the model provided estimates of the transition time scales between these states. On the one hand, the observed AHD conformational variability was expected in light of previous reports stating that the AHD could either not be resolved at high resolution or assumed different orientations in X-ray crystal or cryo-electron microscopy structures of GPCR-G protein complexes,^{18,58–60} as well as inferences from double electron-electron resonance spectroscopy³⁰ and molecular dynamics simulations.³¹ On the other hand, the kinetic model of the conformational transitions of G α s on GTP γ S binding and the atomic details of the most populated conformational states sampled by G α s after GTP binding were unknown until now. Among the most populated G α s conformational ensembles at equilibrium, one consisted of particularly long-lived, unique conformational states that required minutes to convert to the crystallographically known GTP γ S-bound G α s conformation. The observed slow closing of the G α s AHD after GTP binding was unexpected, and confirmation of the existence of long-lived intermediate states in a cellular context will be potentially required using single-molecule imaging techniques. Nevertheless, our finding is of interest when considering the possible effects of long-lived intermediate states on the molecular function of Gs, such as activation cycle kinetics, downstream signaling, or GTPase activity.

As the $G\alpha s$ AHD closing is a very slow process, we hypothesized the existence of a molecule that regulates the closing kinetics by binding to the $G\alpha s$ AHD, and identified MAGE D2 as a $G\alpha s$ AHD-binding partner that accelerates the AHD closing kinetics (Figure 5, step iii-b). The precise mechanism by which MAGE D2 interacts with the long-lived intermediate states of $G\alpha s$ to shorten their lifetime or accelerate AHD closing is unknown but worth investigating, possibly via high-resolution structural determination of the $G\alpha s$ -MAGE D2 complex.

$G\alpha$ binds to various proteins, including GEFs (e.g., GPCRs, Ric-8A, GIV/Girdin, or PLC δ 4b), GAPs (e.g., RGSs), effector proteins (e.g., adenylate cyclases or phospholipase C), and other molecules (e.g., GRKs).^{61–65} Several high-resolution structures of $G\alpha$ in complex with different binding proteins have been published, which all indicate the RD as the main binding interface for these binding partners. For example, RGSs primarily interact with the Switch regions of the RD,^{66–68} although minor interactions are also seen with the AHD when $G\alpha$ is the $G\alpha q$ subtype,⁶⁹ and GEFs and effector proteins almost exclusively interact through the RD.^{49,66,70–73}

To our knowledge, MAGE D2 is the first protein found to interact primarily with a $G\alpha$ AHD, specifically the $G\alpha s$ AHD, and to accelerate its closing, which potentially regulates the G protein activation cycle. Notably, the AHD of different $G\alpha$ subtypes have relatively low sequence identity (approximately 27–42% among the $G\alpha s$, $G\alpha i1$, $G\alpha q$, and $G\alpha 12$ AHDs) compared with that of their RD cores (without αN ; approximately 45–58% identity among the $G\alpha s$, $G\alpha i1$, $G\alpha q$, and $G\alpha 12$ RD cores) (Figure S9). Thus, it is tempting to speculate that the AHD might contribute to the functional selectivity of different $G\alpha$ subtypes via their binding to different AHD-binding proteins. As MAGE D2 is the first identified $G\alpha$ AHD-binding protein, we here coin the name $G\alpha$ AHD Binders (GABs). Further studies are needed to identify GABs for other $G\alpha$ subtypes as well as to understand their molecular functions in G protein signaling.

Limitations of the study

The main limitation of our study is that it does not provide detailed structural information about $G\alpha s$ dissociation from the receptor or $G\beta\gamma$. There are several HDX-MS technical limitations that prevent us from distinguishing the sequence of conformational changes occurring before 5 s of GTP γ S addition. These include the lack of control over protein fragmentation during HDX-MS analysis because of the non-specific nature of pepsin digestion, which makes it impossible to study the dynamic behavior of specific fragments. In addition, various factors, such as the mass spectrometry instrument, the specific settings used, and the properties of the peptide itself, influence the analysis of the resulting peptic peptides. Our enhanced sampling by metadynamics simulations is also limited as it is only focused on the exploration of the separation between AHD and RD. Identifying optimal CVs is another known limitation for metadynamics simulations as it requires testing multiple options before identifying those that lead to smooth convergence of the simulation. An additional caveat of our study is that the timeline monitored in the *in vitro* experimental studies (5 s–30 min) may be different from the timeline required for $G\alpha s$ activation in a cellular context.

STAR★METHODS

Detailed methods are provided in the online version of this paper and include the following:

- KEY RESOURCES TABLE
- RESOURCE AVAILABILITY
 - Lead contact
 - Materials availability
 - Data and code availability
- EXPERIMENTAL MODEL AND SUBJECT DETAILS
- METHOD DETAILS
 - Expression and purification of the β_2 AR
 - Expression and purification of Gs and $G\beta\gamma$
 - Expression and purification of $G\alpha s$, $G\alpha s$ AHD, and MAGE D2 MHD
 - Nucleotide-free β_2 AR–Gs complex formation
 - Pulse-labeling HDX-MS
 - Measurement of the separation between the RD and AHD

- Nucleotide exchange assay
- Y2H assay
- Microscale thermophoresis (MST) assay
- Immunostaining
- Immunoprecipitation and immunoblot analysis
- Systems setup for simulations
- Molecular dynamics simulations for energy minimization and equilibration
- Metadynamics simulations for exhaustive conformational sampling
- Clustering of metadynamics-derived conformational states
- Prediction of protection factors from metadynamics-sampled conformations
- Prediction of quenching data using metadynamics-sampled conformations
- Bayesian inference to update metadynamics-derived prior probabilities of conformational states with pulsed HDX-MS and fluorescence quenching data
- Maximum Caliber priors and sampling to derive the transition matrix
- **QUANTIFICATION AND STATISTICAL ANALYSIS**

SUPPLEMENTAL INFORMATION

Supplemental information can be found online at <https://doi.org/10.1016/j.isci.2023.106603>.

ACKNOWLEDGMENTS

Computations were supported through the computational resources and staff expertise provided by Scientific Computing at the Icahn School of Medicine at Mount Sinai, and were run on resources available through the Office of Research Infrastructure of the National Institutes of Health under award number S10OD026880. The content is solely the responsibility of the authors and does not necessarily represent the official views of the National Institutes of Health. This work was supported by grants from the National Institutes of Health (DA045473 to M.F.) and from the National Research Foundation of Korea funded by the Korean government (NRF-2021R1A2C3003518 and NRF-2019R1A5A2027340 to K.Y.C., and NRF-2019R1C1C1010675 to J.L.).

AUTHOR CONTRIBUTIONS

D.A. analyzed HDX-MS data, developed and performed the TriQ used for measuring the AHD movement, prepared MAGE D2 MHD and G α s AHD, and performed MST analysis. D.P. developed the novel Bayesian integrative modeling framework and used it to derive the proposed kinetic model of G α s activation on GTP γ S binding. N.M.D. prepared GPCR–Gs complexes, performed HDX-MS experiments, and analyzed the mass spectrometry data. J.X. prepared β_2 AR for TriQ. L.S.E. carried out the metadynamics simulations of the nucleotide-free β_2 AR–Gs complex and clustered the simulation results. A.S. carried out the metadynamics simulations of the GTP γ S-bound crystal structure. M.W.Y. prepared constructs for Y2H library screening. J.K., D.G., and J.L. carried out the immunofluorescence and immunoprecipitation assays. Y.D. prepared β_2 AR and Gs for HDX-MS. M.F. and K.Y.C. initiated the project, supervised the research, analyzed the data, and wrote the manuscript with contributions from all authors.

DECLARATION OF INTERESTS

D.A. and K.Y.C. declare a patent application in Korea for the measurement of the separation between the RD and AHD (Korean patent application number: 10-2022-0129136).

INCLUSION AND DIVERSITY

We support inclusive, diverse, and equitable conduct of research.

Received: March 3, 2023

Revised: March 16, 2023

Accepted: March 29, 2023

Published: April 8, 2023

REFERENCES

- Milligan, G., and Kostenis, E. (2006). Heterotrimeric G-proteins: a short history. *Br. J. Pharmacol.* 147, S46–S55. <https://doi.org/10.1038/sj.bjp.0706405>.
- Yang, D., Zhou, Q., Labroska, V., Qin, S., Darbalaei, S., Wu, Y., Yuliantie, E., Xie, L., Tao, H., Cheng, J., et al. (2021). G protein-coupled receptors: structure- and function-based drug discovery. *Signal Transduct. Targeted Ther.* 6, 7. <https://doi.org/10.1038/s41392-020-00435-w>.
- Rogers, K. (2019). *G Protein-Coupled Receptor* (Encyclopedia Britannica).
- Traut, T.W. (1994). Physiological concentrations of purines and pyrimidines. *Mol. Cell. Biochem.* 140, 1–22. <https://doi.org/10.1007/BF00928361>.
- Draper-Joyce, C.J., Khoshouei, M., Thal, D.M., Liang, Y.L., Nguyen, A.T.N., Furness, S.G.B., Venugopal, H., Baltos, J.A., Plietko, J.M., Danev, R., et al. (2018). Structure of the adenosine-bound human adenosine A1 receptor-Gi complex. *Nature* 558, 559–563. <https://doi.org/10.1038/s41586-018-0236-6>.
- García-Nafria, J., Lee, Y., Bai, X., Carpenter, B., and Tate, C.G. (2018). Cryo-EM structure of the adenosine A2A receptor coupled to an engineered heterotrimeric G protein. *Elife* 7, e35946. <https://doi.org/10.7554/eLife.35946>.
- García-Nafria, J., Nehmé, R., Edwards, P.C., and Tate, C.G. (2018). Cryo-EM structure of the serotonin 5-HT1B receptor coupled to heterotrimeric Go. *Nature* 558, 620–623. <https://doi.org/10.1038/s41586-018-0241-9>.
- Kang, Y., Kuybeda, O., de Waal, P.W., Mukherjee, S., Van Eps, N., Dutka, P., Zhou, X.E., Bartesaghi, A., Erramilli, S., Morizumi, T., et al. (2018). Cryo-EM structure of human rhodopsin bound to an inhibitory G protein. *Nature* 558, 553–558. <https://doi.org/10.1038/s41586-018-0215-y>.
- Kato, H.E., Zhang, Y., Hu, H., Suomivuori, C.M., Kadji, F.M.N., Aoki, J., Krishna Kumar, K., Fonseca, R., Hilger, D., Huang, W., et al. (2019). Conformational transitions of a neurotensin receptor 1-Gi1 complex. *Nature* 572, 80–85. <https://doi.org/10.1038/s41586-019-1337-6>.
- Koehl, A., Hu, H., Maeda, S., Zhang, Y., Qu, Q., Paggi, J.M., Latorraca, N.R., Hilger, D., Dawson, R., Matile, H., et al. (2018). Structure of the micro-opioid receptor-Gi protein complex. *Nature* 558, 547–552. <https://doi.org/10.1038/s41586-018-0219-7>.
- Krishna Kumar, K., Shalev-Benami, M., Robertson, M.J., Hu, H., Banister, S.D., Hollingsworth, S.A., Latorraca, N.R., Kato, H.E., Hilger, D., Maeda, S., et al. (2019). Structure of a signaling cannabinoid receptor 1-G protein complex. *Cell* 176, 448–458.e12. <https://doi.org/10.1016/j.cell.2018.11.040>.
- Maeda, S., Qu, Q., Robertson, M.J., Skiniotis, G., and Kobilka, B.K. (2019). Structures of the M1 and M2 muscarinic acetylcholine receptor/G-protein complexes. *Science* 364, 552–557. <https://doi.org/10.1126/science.aaw5188>.
- Qi, X., Liu, H., Thompson, B., McDonald, J., Zhang, C., and Li, X. (2019). Cryo-EM structure of oxysterol-bound human smoothened coupled to a heterotrimeric Gi. *Nature* 571, 279–283. <https://doi.org/10.1038/s41586-019-1286-0>.
- Tsai, C.J., Marino, J., Adaixo, R., Pamula, F., Muehle, J., Maeda, S., Flock, T., Taylor, N.M., Mohammed, I., Matile, H., et al. (2019). Cryo-EM structure of the rhodopsin-Galphai-beta gamma complex reveals binding of the rhodopsin C-terminal tail to the Gbeta subunit. *Elife* 8, e46041. <https://doi.org/10.7554/eLife.46041>.
- Tsai, C.J., Pamula, F., Nehmé, R., Mühle, J., Weinert, T., Flock, T., Nogly, P., Edwards, P.C., Carpenter, B., Gruhl, T., et al. (2018). Crystal structure of rhodopsin in complex with a mini-Go sheds light on the principles of G protein selectivity. *Sci. Adv.* 4, eaat7052. <https://doi.org/10.1126/sciadv.aat7052>.
- Xing, C., Zhuang, Y., Xu, T.H., Feng, Z., Zhou, X.E., Chen, M., Wang, L., Meng, X., Xue, Y., Wang, J., et al. (2020). Cryo-EM structure of the human cannabinoid receptor CB2-gi signaling complex. *Cell* 180, 645–654.e13. <https://doi.org/10.1016/j.cell.2020.01.007>.
- Zhuang, Y., Liu, H., Edward Zhou, X., Kumar Verma, R., de Waal, P.W., Jang, W., Xu, T.H., Wang, L., Meng, X., Zhao, G., et al. (2020). Structure of formylpeptide receptor 2-Gi complex reveals insights into ligand recognition and signaling. *Nat. Commun.* 11, 885. <https://doi.org/10.1038/s41467-020-14728-9>.
- Rasmussen, S.G.F., DeVree, B.T., Zou, Y., Kruse, A.C., Chung, K.Y., Kobilka, T.S., Thian, F.S., Chae, P.S., Pardon, E., Calinski, D., et al. (2011). Crystal structure of the beta2 adrenergic receptor-Gs protein complex. *Nature* 477, 549–555. <https://doi.org/10.1038/nature10361>.
- Coleman, D.E., Berghuis, A.M., Lee, E., Linder, M.E., Gilman, A.G., and Sprang, S.R. (1994). Structures of active conformations of Gi alpha 1 and the mechanism of GTP hydrolysis. *Science* 265, 1405–1412. <https://doi.org/10.1126/science.8073283>.
- Liu, X., Xu, X., Hilger, D., Aschauer, P., Tiemann, J.K.S., Du, Y., Liu, H., Hirata, K., Sun, X., Guixà-González, R., et al. (2019). Structural insights into the process of GPCR-G protein complex formation. *Cell* 177, 1243–1251.e12. <https://doi.org/10.1016/j.cell.2019.04.021>.
- Sondek, J., Lambright, D.G., Noel, J.P., Hamm, H.E., and Sigler, P.B. (1994). GTPase mechanism of G proteins from the 1.7-Å crystal structure of transducin alpha-GDP-AIF-4. *Nature* 372, 276–279. <https://doi.org/10.1038/372276a0>.
- Sunahara, R.K., Tesmer, J.J., Gilman, A.G., and Sprang, S.R. (1997). Crystal structure of the adenylyl cyclase activator Gsalpha. *Science* 278, 1943–1947. <https://doi.org/10.1126/science.278.5345.1943>.
- Wall, M.A., Coleman, D.E., Lee, E., Iñiguez-Lluhi, J.A., Posner, B.A., Gilman, A.G., and Sprang, S.R. (1995). The structure of the G protein heterotrimer Gi alpha 1 beta 1 gamma 2. *Cell* 83, 1047–1058. [https://doi.org/10.1016/0092-8674\(95\)90220-1](https://doi.org/10.1016/0092-8674(95)90220-1).
- Preininger, A.M., Meiler, J., and Hamm, H.E. (2013). Conformational flexibility and structural dynamics in GPCR-mediated G protein activation: a perspective. *J. Mol. Biol.* 425, 2288–2298. <https://doi.org/10.1016/j.jmb.2013.04.011>.
- García-Nafria, J., and Tate, C.G. (2019). Cryo-EM structures of GPCRs coupled to gs, gi and go. *Mol. Cell. Endocrinol.* 488, 1–13. <https://doi.org/10.1016/j.mce.2019.02.006>.
- Glukhova, A., Draper-Joyce, C.J., Sunahara, R.K., Christopoulos, A., Wootten, D., and Sexton, P.M. (2018). Rules of engagement: GPCRs and G proteins. *ACS Pharmacol. Transl. Sci.* 1, 73–83. <https://doi.org/10.1021/acspstci.8b00026>.
- Du, Y., Duc, N.M., Rasmussen, S.G.F., Hilger, D., Kubiak, X., Wang, L., Bohon, J., Kim, H.R., Wegrecki, M., Asuru, A., et al. (2019). Assembly of a GPCR-G protein complex. *Cell* 177, 1232–1242.e11. <https://doi.org/10.1016/j.cell.2019.04.022>.
- Ham, D., Ahn, D., Ashim, J., Cho, Y., Kim, H.R., Yu, W., and Chung, K.Y. (2021). Conformational switch that induces GDP release from Gi. *J. Struct. Biol.* 213, 107694. <https://doi.org/10.1016/j.jsb.2020.107694>.
- Westfield, G.H., Rasmussen, S.G.F., Su, M., Dutta, S., DeVree, B.T., Chung, K.Y., Calinski, D., Velez-Ruiz, G., Oleskie, A.N., Pardon, E., et al. (2011). Structural flexibility of the G alpha s alpha-helical domain in the beta2-adrenoceptor Gs complex. *Proc. Natl. Acad. Sci. USA* 108, 16086–16091. <https://doi.org/10.1073/pnas.1113645108>.
- Van Eps, N., Preininger, A.M., Alexander, N., Kaya, A.I., Meier, S., Meiler, J., Hamm, H.E., and Hubbell, W.L. (2011). Interaction of a G protein with an activated receptor opens the interdomain interface in the alpha subunit. *Proc. Natl. Acad. Sci. USA* 108, 9420–9424. <https://doi.org/10.1073/pnas.1105810108>.
- Dror, R.O., Mildorf, T.J., Hilger, D., Manglik, A., Borhani, D.W., Arlow, D.H., Philippsen, A., Villanueva, N., Yang, Z., Lerch, M.T., et al. (2015). SIGNAL TRANSDUCTION. Structural basis for nucleotide exchange in heterotrimeric G proteins. *Science* 348, 1361–1365. <https://doi.org/10.1126/science.aaa5264>.
- Ahn, D., Ham, D., and Chung, K.Y. (2021). The conformational transition during G protein-coupled receptor (GPCR) and G protein interaction. *Curr. Opin. Struct. Biol.* 69, 117–123. <https://doi.org/10.1016/j.sbi.2021.03.013>.

33. Kim, K., Paulekas, S., Sadler, F., Gupte, T.M., Ritt, M., Dysthe, M., Vaidehi, N., and Sivaramakrishnan, S. (2021). beta2-adrenoceptor ligand efficacy is tuned by a two-stage interaction with the Galphas C terminus. *Proc. Natl. Acad. Sci. USA* **118**. e2017201118. <https://doi.org/10.1073/pnas.2017201118>.
34. Sun, X., Singh, S., Blumer, K.J., and Bowman, G.R. (2018). Simulation of spontaneous G protein activation reveals a new intermediate driving GDP unbinding. *Elife* **7**, e38465. <https://doi.org/10.7554/eLife.38465>.
35. Barducci, A., Bussi, G., and Parrinello, M. (2008). Well-tempered metadynamics: a smoothly converging and tunable free-energy method. *Phys. Rev. Lett.* **100**, 020603. <https://doi.org/10.1103/PhysRevLett.100.020603>.
36. Rout, M.P., and Sali, A. (2019). Principles for integrative structural biology studies. *Cell* **177**, 1384–1403. <https://doi.org/10.1016/j.cell.2019.05.016>.
37. Dixit, P.D., Jain, A., Stock, G., and Dill, K.A. (2015). Inferring transition rates of networks from populations in continuous-time Markov processes. *J. Chem. Theor. Comput.* **11**, 5464–5472. <https://doi.org/10.1021/acs.jctc.5b00537>.
38. Dixit, P.D., and Dill, K.A. (2014). Inferring microscopic kinetic rates from stationary state distributions. *J. Chem. Theor. Comput.* **10**, 3002–3005. <https://doi.org/10.1021/ct5001389>.
39. Pérez-Hernández, G., Paul, F., Giorgino, T., De Fabritiis, G., and Noé, F. (2013). Identification of slow molecular order parameters for Markov model construction. *J. Chem. Phys.* **139**, 015102. <https://doi.org/10.1063/1.4811489>.
40. Schwantes, C.R., and Pande, V.S. (2013). Improvements in Markov state model construction reveal many non-native interactions in the folding of NTL9. *J. Chem. Theor. Comput.* **9**, 2000–2009. <https://doi.org/10.1021/ct300878a>.
41. E, W., and Vanden-Eijnden, E. (2010). Transition-path theory and path-finding algorithms for the study of rare events. *Annu. Rev. Phys. Chem.* **61**, 391–420. <https://doi.org/10.1146/annurev.physchem.040808.090412>.
42. Harrison, R.A., and Engen, J.R. (2016). Conformational insight into multi-protein signaling assemblies by hydrogen-deuterium exchange mass spectrometry. *Curr. Opin. Struct. Biol.* **41**, 187–193. <https://doi.org/10.1016/j.sbi.2016.08.003>.
43. Chung, K.Y., Rasmussen, S.G.F., Liu, T., Li, S., DeVree, B.T., Chae, P.S., Calinski, D., Kobilka, B.K., Woods, V.L., Jr., and Sunahara, R.K. (2011). Conformational changes in the G protein Gs induced by the beta2 adrenergic receptor. *Nature* **477**, 611–615. <https://doi.org/10.1038/nature10488>.
44. Kim, H.R., Xu, J., Maeda, S., Duc, N.M., Ahn, D., Du, Y., and Chung, K.Y. (2020). Structural mechanism underlying primary and secondary coupling between GPCRs and the Gi/o family. *Nat. Commun.* **11**, 3160. <https://doi.org/10.1038/s41467-020-16975-2>.
45. Jones Brunette, A.M., and Farrens, D.L. (2014). Distance mapping in proteins using fluorescence spectroscopy: tyrosine, like tryptophan, quenches bimane fluorescence in a distance-dependent manner. *Biochemistry* **53**, 6290–6301. <https://doi.org/10.1021/bi500493r>.
46. Focia, P.J., Alam, H., Lu, T., Ramirez, U.D., and Freymann, D.M. (2004). Novel protein and Mg2+ configurations in the Mg2+GDP complex of the SRP GTPase ffh. *Proteins* **54**, 222–230. <https://doi.org/10.1002/prot.10598>.
47. Best, R.B., and Vendruscolo, M. (2006). Structural interpretation of hydrogen exchange protection factors in proteins: characterization of the native state fluctuations of C12. *Structure* **14**, 97–106. <https://doi.org/10.1016/j.str.2005.09.012>.
48. Kach, J., Sethakorn, N., and Dulin, N.O. (2012). A finer tuning of G-protein signaling through regulated control of RGS proteins. *Am. J. Physiol. Heart Circ. Physiol.* **303**, H19–H35. <https://doi.org/10.1152/ajpheart.00764.2011>.
49. Kalogiropoulos, N.A., Rees, S.D., Ngo, T., Kopcho, N.J., Ilatovskiy, A.V., Sun, N., Komives, E.A., Chang, G., Ghosh, P., and Kufareva, I. (2019). Structural basis for GPCR-independent activation of heterotrimeric Gi proteins. *Proc. Natl. Acad. Sci. U S A* **116**, 16394–16403. <https://doi.org/10.1073/pnas.1906658116>.
50. Siderovski, D.P., and Willard, F.S. (2005). The GAPs, GEFs, and GDIs of heterotrimeric G-protein alpha subunits. *Int. J. Biol. Sci.* **1**, 51–66. <https://doi.org/10.7150/ijbs.1.51>.
51. Srivastava, D., and Artemyev, N.O. (2020). Ric-8A, a GEF, and a chaperone for G protein alpha-subunits: evidence for the two-faced interface. *Bioessays* **42**, e1900208. <https://doi.org/10.1002/bies.201900208>.
52. Srivastava, D., Gakhar, L., and Artemyev, N.O. (2019). Structural underpinnings of Ric8A function as a G-protein alpha-subunit chaperone and guanine-nucleotide exchange factor. *Nat. Commun.* **10**, 3084. <https://doi.org/10.1038/s41467-019-11088-x>.
53. Laghmani, K., Beck, B.B., Yang, S.S., Seayfan, E., Wenzel, A., Reusch, B., Vitzthum, H., Priem, D., Demaretz, S., Bergmann, K., et al. (2016). Polyhydramnios, transient antenatal Bartter's syndrome, and MAGED2 mutations. *N. Engl. J. Med.* **374**, 1853–1863. <https://doi.org/10.1056/NEJMoa1507629>.
54. Paek, J., Kalocsay, M., Staus, D.P., Wingler, L., Pascolutti, R., Paulo, J.A., Gygi, S.P., and Kruse, A.C. (2017). Multidimensional tracking of GPCR signaling via peroxidase-catalyzed proximity labeling. *Cell* **169**, 338–349.e11. <https://doi.org/10.1016/j.cell.2017.03.028>.
55. Reusch, B., Bartram, M.P., Dafinger, C., Palacio-Escat, N., Wenzel, A., Fenton, R.A., Saez-Rodriguez, J., Schermer, B., Benzing, T., Altmüller, J., et al. (2022). MAGED2 controls vasopressin-induced aquaporin-2 expression in collecting duct cells. *J. Proteomics* **252**, 104424. <https://doi.org/10.1016/j.jprot.2021.104424>.
56. Doyle, J.M., Gao, J., Wang, J., Yang, M., and Potts, P.R. (2010). MAGE-RING protein complexes comprise a family of E3 ubiquitin ligases. *Mol. Cell* **39**, 963–974. <https://doi.org/10.1016/j.molcel.2010.08.029>.
57. Newman, J.A., Cooper, C.D.O., Roos, A.K., Aitkenhead, H., Oppermann, U.C.T., Cho, H.J., Osman, R., and Gileadi, O. (2016). Structures of two melanoma-associated antigens suggest allosteric regulation of effector binding. *PLoS One* **11**, e0148762. <https://doi.org/10.1371/journal.pone.0148762>.
58. Duan, J., Xu, P., Cheng, X., Mao, C., Croll, T., He, X., Shi, J., Luan, X., Yin, W., You, E., et al. (2021). Structures of full-length glycoprotein hormone receptor signalling complexes. *Nature* **598**, 688–692. <https://doi.org/10.1038/s41586-021-03924-2>.
59. Sun, B., Feng, D., Chu, M.L.H., Fish, I., Lovera, S., Sands, Z.A., Kelm, S., Valade, A., Wood, M., Ceska, T., et al. (2021). Crystal structure of dopamine D1 receptor in complex with G protein and a non-catechol agonist. *Nat. Commun.* **12**, 3305. <https://doi.org/10.1038/s41467-021-23519-9>.
60. Zhang, X., Belousoff, M.J., Zhao, P., Kooistra, A.J., Truong, T.T., Ang, S.Y., Underwood, C.R., Egebjerg, T., Senel, P., Stewart, G.D., et al. (2020). Differential GLP-1R binding and activation by peptide and non-peptide agonists. *Mol. Cell* **80**, 485–500.e7. <https://doi.org/10.1016/j.molcel.2020.09.020>.
61. Baltoumas, F.A., Theodoropoulou, M.C., and Hamodrakas, S.J. (2013). Interactions of the alpha-subunits of heterotrimeric G-proteins with GPCRs, effectors and RGS proteins: a critical review and analysis of interacting surfaces, conformational shifts, structural diversity and electrostatic potentials. *J. Struct. Biol.* **182**, 209–218. <https://doi.org/10.1016/j.jsb.2013.03.004>.
62. Ghosh, P., and Garcia-Marcos, M. (2020). Do all roads lead to rome in G-protein activation? *Trends Biochem. Sci.* **45**, 182–184. <https://doi.org/10.1016/j.tibs.2019.10.010>.
63. Maziarz, M., Broselid, S., DiGiacomo, V., Park, J.C., Luebbbers, A., Garcia-Navarrete, L., Blanco-Canosa, J.B., Baillie, G.S., and Garcia-Marcos, M. (2018). A biochemical and genetic discovery pipeline identifies PLCdelta4b as a nonreceptor activator of heterotrimeric G-proteins. *J. Biol. Chem.* **293**, 16964–16983. <https://doi.org/10.1074/jbc.RA118.003580>.

64. Syrovatkina, V., Alegre, K.O., Dey, R., and Huang, X.Y. (2016). Regulation, signaling, and physiological functions of G-proteins. *J. Mol. Biol.* 428, 3850–3868. <https://doi.org/10.1016/j.jmb.2016.08.002>.
65. Tesmer, J.J., Sunahara, R.K., Gilman, A.G., and Sprang, S.R. (1997). Crystal structure of the catalytic domains of adenyl cyclase in a complex with G α . *Science* 278, 1907–1916. <https://doi.org/10.1126/science.278.5345.1907>.
66. Slep, K.C., Kercher, M.A., He, W., Cowan, C.W., Wensel, T.G., and Sigler, P.B. (2001). Structural determinants for regulation of phosphodiesterase by a G protein at 2.0 Å. *Nature* 409, 1071–1077. <https://doi.org/10.1038/35059138>.
67. Soundararajan, M., Willard, F.S., Kimple, A.J., Turnbull, A.P., Ball, L.J., Schoch, G.A., Gileadi, C., Fedorov, O.Y., Dowler, E.F., Higman, V.A., et al. (2008). Structural diversity in the RGS domain and its interaction with heterotrimeric G protein α -subunits. *Proc. Natl. Acad. Sci. USA* 105, 6457–6462. <https://doi.org/10.1073/pnas.0801508105>.
68. Tesmer, J.J., Berman, D.M., Gilman, A.G., and Sprang, S.R. (1997). Structure of RGS4 bound to AlF $_4$ -activated G(i α 1): stabilization of the transition state for GTP hydrolysis. *Cell* 89, 251–261. [https://doi.org/10.1016/s0092-8674\(00\)80204-4](https://doi.org/10.1016/s0092-8674(00)80204-4).
69. Nance, M.R., Kreutz, B., Tesmer, V.M., Sterne-Marr, R., Kozasa, T., and Tesmer, J.J.G. (2013). Structural and functional analysis of the regulator of G protein signaling 2-galphaq complex. *Structure* 21, 438–448. <https://doi.org/10.1016/j.str.2012.12.016>.
70. Lutz, S., Shankaranarayanan, A., Coco, C., Ridilla, M., Nance, M.R., Vettel, C., Baltus, D., Evelyn, C.R., Neubig, R.R., Wieland, T., and Tesmer, J.J.G. (2007). Structure of Galphaq-p63RhoGEF-RhoA complex reveals a pathway for the activation of RhoA by GPCRs. *Science* 318, 1923–1927. <https://doi.org/10.1126/science.1147554>.
71. McClelland, L.J., Zhang, K., Mou, T.C., Johnston, J., Yates-Hansen, C., Li, S., Thomas, C.J., Doukov, T.I., Triest, S., Wohlkonig, A., et al. (2020). Structure of the G protein chaperone and guanine nucleotide exchange factor Ric-8A bound to Galpha1. *Nat. Commun.* 11, 1077. <https://doi.org/10.1038/s41467-020-14943-4>.
72. Qi, C., Sorrentino, S., Medalia, O., and Korkhov, V.M. (2019). The structure of a membrane adenyl cyclase bound to an activated stimulatory G protein. *Science* 364, 389–394. <https://doi.org/10.1126/science.aav0778>.
73. Waldo, G.L., Ricks, T.K., Hicks, S.N., Cheever, M.L., Kawano, T., Tsuboi, K., Wang, X., Montell, C., Kozasa, T., Sondek, J., and Harden, T.K. (2010). Kinetic scaffolding mediated by a phospholipase C-beta and Gq signaling complex. *Science* 330, 974–980. <https://doi.org/10.1126/science.1193438>.
74. Rosenbaum, D.M., Cherezov, V., Hanson, M.A., Rasmussen, S.G.F., Thian, F.S., Kobilka, T.S., Choi, H.J., Yao, X.J., Weis, W.I., Stevens, R.C., and Kobilka, B.K. (2007). GPCR engineering yields high-resolution structural insights into beta2-adrenergic receptor function. *Science* 318, 1266–1273. <https://doi.org/10.1126/science.1156009>.
75. Schrodinger Release 2019-4 (2019) (Schrodinger, LLC).
76. Martí-Renom, M.A., Stuart, A.C., Fiser, A., Sánchez, R., Melo, F., and Sali, A. (2000). Comparative protein structure modeling of genes and genomes. *Annu. Rev. Biophys. Biomol. Struct.* 29, 291–325. <https://doi.org/10.1146/annurev.biophys.29.1.291>.
77. Webb, B., and Sali, A. (2016). Comparative protein structure modeling using MODELLER. *Curr. Protoc. Protein Sci.* 86, 2.9.1–2.9.37. <https://doi.org/10.1002/cpps.20>.
78. Vanommeslaeghe, K., Hatcher, E., Acharya, C., Kundu, S., Zhong, S., Shim, J., Darian, E., Guvench, O., Lopes, P., Vorobyov, I., and Mackerell, A.D., Jr. (2010). CHARMM general force field: a force field for drug-like molecules compatible with the CHARMM all-atom additive biological force fields. *J. Comput. Chem.* 31, 671–690. <https://doi.org/10.1002/jcc.21367>.
79. Jorgensen, W.L., Chandrasekhar, J., Madura, J.D., Impey, R.W., and Klein, M.L. (1983). Comparison of simple potential functions for simulating liquid water. *J. Chem. Phys.* 79, 926–935. <https://doi.org/10.1063/1.445869>.
80. Huang, J., Rauscher, S., Nawrocki, G., Ran, T., Feig, M., de Groot, B.L., Grubmüller, H., and Mackerell, A.D., Jr. (2017). CHARMM36m: an improved force field for folded and intrinsically disordered proteins. *Nat. Methods* 14, 71–73.
81. Yoo, J., and Aksimentiev, A. (2012). Improved parametrization of Li $^+$, Na $^+$, K $^+$, and Mg $^{2+}$ ions for all-atom molecular dynamics simulations of nucleic acid systems. *J. Phys. Chem. Lett.* 3, 45–50. <https://doi.org/10.1021/jz201501a>.
82. Darden, T., York, D., and Pedersen, L. (1993). Particle mesh Ewald - an N.log(N) method for Ewald sums in large systems. *J. Chem. Phys.* 98, 10089–10092. <https://doi.org/10.1063/1.464397>.
83. Hess, B., Bekker, H., Berendsen, H.J.C., and Fraaije, J. (1997). LINCS: a linear constraint solver for molecular simulations. *J. Comput. Chem.* 18, 1463–1472. [https://doi.org/10.1002/\(Sici\)1096-987x\(199709\)18:12<1463::Aid-Jcc4>3.3.Co;2-L](https://doi.org/10.1002/(Sici)1096-987x(199709)18:12<1463::Aid-Jcc4>3.3.Co;2-L).
84. Feenstra, K.A., Hess, B., and Berendsen, H.J.C. (1999). Improving efficiency of large time-scale molecular dynamics simulations of hydrogen-rich systems. *J. Comput. Chem.* 20, 786–798.
85. Nosé, S. (1984). A molecular-dynamics method for simulations in the canonical ensemble. *Mol. Phys.* 52, 255–268. <https://doi.org/10.1080/00268978400101201>.
86. Hoover, W.G. (1985). Canonical dynamics - equilibrium phase-space distributions. *Phys. Rev.* 31, 1695–1697. <https://doi.org/10.1103/PhysRevA.31.1695>.
87. Parrinello, M., and Rahman, A. (1981). Polymorphic transitions in single-crystals - a new molecular-dynamics method. *J. Appl. Phys.* 52, 7182–7190. <https://doi.org/10.1063/1.328693>.
88. Nosé, S., and Klein, M.L. (1983). Constant pressure molecular-dynamics for molecular-systems. *Mol. Phys.* 50, 1055–1076. <https://doi.org/10.1080/00268978300102851>.
89. Abraham, M.J., Murtola, T., Schulz, R., Páll, S., Smith, J.C., Hess, B., and Lindahl, E. (2015). GROMACS: high performance molecular simulations through multi-level parallelism from laptops to supercomputers. *SoftwareX* 1–2, 19–25.
90. Klauda, J.B., Venable, R.M., Freites, J.A., O'Connor, J.W., Tobias, D.J., Mondragon-Ramirez, C., Vorobyov, I., MacKerell, A.D., Jr., and Pastor, R.W. (2010). Update of the CHARMM all-atom additive force field for lipids: validation on six lipid types. *J. Phys. Chem. B* 114, 7830–7843. <https://doi.org/10.1021/jp101759q>.
91. Mark, P., and Nilsson, L. (2001). Structure and dynamics of the TIP3P, SPC, and SPC/E water models at 298 K. *J. Phys. Chem. A* 105, 9954–9960.
92. Laio, A., and Gervasio, F.L. (2008). Metadynamics: a method to simulate rare events and reconstruct the free energy in biophysics, chemistry and material science. *Rep. Prog. Phys.* 71, 126601. <https://doi.org/10.1088/0034-4885/71/12/126601>.
93. Laio, A., and Parrinello, M. (2002). Escaping free-energy minima. *Proc. Natl. Acad. Sci. USA* 99, 12562–12566. <https://doi.org/10.1073/pnas.202427399>.
94. Bonomi, M., Branduardi, D., Bussi, G., Camilloni, C., Provasi, D., Raiteri, P., Donadio, D., Marinelli, F., Pietrucci, F., Broglia, R.A., and Parrinello, M. (2009). PLUMED: a portable plugin for free-energy calculations with molecular dynamics. *Comput. Phys. Commun.* 180, 1961–1972. <https://doi.org/10.1016/j.cpc.2009.05.011>.
95. Tribello, G.A., Bonomi, M., Branduardi, D., Camilloni, C., and Bussi, G. (2014). Plumed 2: new feathers for an old bird. *Comput. Phys. Commun.* 185, 604–613. <https://doi.org/10.1016/j.cpc.2013.09.018>.
96. Tiwary, P., and Parrinello, M. (2015). A time-independent free energy estimator for metadynamics. *J. Phys. Chem. B* 119, 736–742. <https://doi.org/10.1021/jp504920s>.
97. McGibbon, R.T., Beauchamp, K.A., Harrigan, M.P., Klein, C., Swails, J.M., Hernández, C.X., Schwantes, C.R., Wang, L.P., Lane, T.J., and Pantaleo, V.S. (2015). MDTraj: a modern open library for the analysis of molecular dynamics trajectories. *Biophys. J.* 109, 1528–1532. <https://doi.org/10.1016/j.bpj.2015.08.015>.

98. Scherer, M.K., Trendelkamp-Schroer, B., Paul, F., Pérez-Hernández, G., Hoffmann, M., Plattner, N., Wehmeyer, C., Prinz, J.H., and Noé, F. (2015). PyEMMA 2: a software package for estimation, validation, and analysis of Markov models. *J. Chem. Theor. Comput.* *11*, 5525–5542. <https://doi.org/10.1021/acs.jctc.5b00743>.
99. Bai, Y., Milne, J.S., Mayne, L., and Englander, S.W. (1993). Primary structure effects on peptide group hydrogen exchange. *Proteins* *17*, 75–86. <https://doi.org/10.1002/prot.340170110>.
100. Molday, R.S., Englander, S.W., and Kallen, R.G. (1972). Primary structure effects on peptide group hydrogen exchange. *Biochemistry* *11*, 150–158. <https://doi.org/10.1021/bi00752a003>.
101. Kim, P.S., and Baldwin, R.L. (1982). Influence of charge on the rate of amide proton exchange. *Biochemistry* *21*, 1–5. <https://doi.org/10.1021/bi00530a001>.
102. Wu, K.P., Weinstock, D.S., Narayanan, C., Levy, R.M., and Baum, J. (2009). Structural reorganization of alpha-synuclein at low pH observed by NMR and REMD simulations. *J. Mol. Biol.* *391*, 784–796. <https://doi.org/10.1016/j.jmb.2009.06.063>.
103. Vendruscolo, M., Paci, E., Dobson, C.M., and Karplus, M. (2003). Rare fluctuations of native proteins sampled by equilibrium hydrogen exchange. *J. Am. Chem. Soc.* *125*, 15686–15687. <https://doi.org/10.1021/ja036523z>.
104. Wan, H., Ge, Y., Razavi, A., and Voelz, V.A. (2020). Reconciling simulated ensembles of apomyoglobin with experimental hydrogen/deuterium exchange data using bayesian inference and multiensemble Markov state models. *J. Chem. Theor. Comput.* *16*, 1333–1348. <https://doi.org/10.1021/acs.jctc.9b01240>.
105. Callis, P.R. (2014). Binding phenomena and fluorescence quenching. II: photophysics of aromatic residues and dependence of fluorescence spectra on protein conformation. *J. Mol. Struct.* *1077*, 22–29.
106. Mansoor, S.E., Dewitt, M.A., and Farrens, D.L. (2010). Distance mapping in proteins using fluorescence spectroscopy: the tryptophan-induced quenching (TriQ) method. *Biochemistry* *49*, 9722–9731. <https://doi.org/10.1021/bi100907m>.
107. Mansoor, S.E., McHaourab, H.S., and Farrens, D.L. (2002). Mapping proximity within proteins using fluorescence spectroscopy. A study of T4 lysozyme showing that tryptophan residues quench bimane fluorescence. *Biochemistry* *41*, 2475–2484. <https://doi.org/10.1021/bi011198i>.
108. Pressé, S., Ghosh, K., Lee, J., and Dill, K.A. (2013). Principles of maximum entropy and maximum caliber in statistical physics. *Rev. Mod. Phys.* *85*, 1115–1141.
109. Caticha, A., and Preuss, R. (2004). Maximum entropy and Bayesian data analysis: Entropic prior distributions. *Phys. Rev. E Stat. Nonlin. Soft Matter Phys.* *70*, 046127. <https://doi.org/10.1103/PhysRevE.70.046127>.

STAR★METHODS

KEY RESOURCES TABLE

REAGENT or RESOURCE	SOURCE	IDENTIFIER
Chemicals, peptides, and recombinant proteins		
Anti-BCG1 antibody	Abcam	Cat# ab236592
GTP γ S	Abcam	Cat# ab146662
DDM detergent	Anatrace	Cat# D310
Skim milk	BD Life Science	Cat# 232100
SureBeads protein G magnetic beads	Bio-Rad	Cat# 161-4023
Protease inhibitor cocktail	BioVision	Cat# K272
Deuterium oxide	Cambridge isotope laboratories	Cat# DLM-11-100
Anti-Mouse IgG HRP-linked antibody	Cell Signaling	Cat# 7076S
Anti-Rabbit IgG HRP-linked antibody	Cell Signaling	Cat# 7074S
BI-167107	Custom	N/A
3X FLAG peptide	Custom	N/A
Ni-NTA resin	Cytiva	Cat# 17057501
Dimethyl sulfoxide	Duchefa	Cat# D1370
Bestbac cotransfection kit	Expression Systems	Cat# 91-200
ESF921 culture medium	Expression Systems	Cat# 96-001
Xpert protease inhibitor cocktail	GenDEPOT	Cat# P3200
Leupeptin	Goldbio	Cat# L-010
Lysozyme	Goldbio	Cat# L-040
TCEP	Goldbio	Cat# TCEP
IPTG	Goldbio	Cat# I2481C
Goat anti-mouse IgG 2nd antibody, Alexa Fluor 647	Invitrogen	Cat# A-21235; RRID: AB_2535804
HOECHST 33342	Invitrogen	Cat# H3570
Lipofectamine 3000 transfection reagent	Invitrogen	Cat# L3000001
Pepsin column	Life Technologies	Cat# 2313100
Anti-FLAG M2 magnetic beads	Millipore	Cat# M8823
Apyrase	NEB	Cat# M0398
Premium capillaries	NanoTemper	Cat# MO-L011
Monolith protein labeling kit RED-NHS	NanoTemper	Cat# MO-K025
Mouse monoclonal TurboGFP antibody	Origene	Cat# TA150041; RRID: AB_2622256
DNase I	Roche	Cat# 11284932001
Bovine serum albumin (BSA)	Roche	Cat# 10735086001
Alprenolol	Sigma-Aldrich	Cat# A0360000
Ammonium persulfate	Sigma-Aldrich	Cat# A3678
Anti-FLAG M1 affinity resin	Sigma-Aldrich	Cat# A4596
Benzamidine	Sigma-Aldrich	Cat# 12072
Cholesteryl hemisuccinate	Sigma-Aldrich	Cat# C6512
GDP	Sigma-Aldrich	Cat# G7127
Imidazole	Sigma-Aldrich	Cat# I2399
Monobromobimane	Sigma-Aldrich	Cat# B4380
Monoclonal ANTI-FLAG M2 antibody	Sigma-Aldrich	Cat# F1804; RRID: AB_262044

(Continued on next page)

Continued

REAGENT or RESOURCE	SOURCE	IDENTIFIER
Nonidet P 40 Substitute	Sigma-Aldrich	Cat# 74385
Phenylmethylsulfonyl fluoride	Sigma-Aldrich	Cat# P7626
Triton X-100	Sigma-Aldrich	Cat# X100
Pierce 16% formaldehyde	ThermoFisher Scientific	Cat# 28906
D-PBS	Welgene	Cat# LB 001-02
Fetal Bovine Serum (FBS)	Welgene	Cat# S 001-07
Penicillin-Streptomycin Solution (100X)	Welgene	Cat# LM 011-01
RPMI 1640 Medium (1X)	Welgene	Cat# LM 011-01
TOM Transfection Optimized Medium	Welgene	Cat# TR 004-01
Trypsin-EDTA Solution (10X)	Welgene	Cat# LS 015-02

Biological samples

HEK293T	ATCC	Cat# CRL-3216
<i>E. coli</i> DH5 α Chemically Competent	Enzynomics	Cat# CP010
Insect cell line Sf9	Expression Systems	Cat# 94-001F
Insect cell line Tni	Expression Systems	Cat# 94-002F
<i>E. coli</i> LOBSTR-BL21(DE3)	Kerafast	Cat# EC1001

Recombinant DNA

pVL1392-wt β_2 AR	This study	N/A
pVL1392duet-G $\beta\gamma$	This study	N/A
pET28a-G α_s /mutants	This study	N/A
pET28a-MAGE D2 MHD	This study	N/A
pET28a-G α_s AHD	This study	N/A
pCMV-WT G α_s AHD-3X FLAG	This study	N/A
pCMV-WT G α_s -3X FLAG	This study	N/A
MAGE D2 Human Tagged ORF Clone	Origene	Cat# RG214066/A

Software and algorithms

Prism 6.0	Graphpad	graphpad.com
PyMol 2.3	Schrodinger	pymol.org
Maestro2019-4	Schrodinger	www.schrodinger.com
Proteinlynx Global Server 2.4	Waters	www.waters.com
DynamX 3.0	Waters	www.waters.com
MO.Control 1.6	NanoTemper	nanotempertech.com
MO.Affinity Analysis 2.3	NanoTemper	nanotempertech.com
ImageJ/Fiji	National Institutes of Health	imagej.net
LAS X	Leica Microsystems	leica-microsystems.com
MODELLER 9.19	Sali Lab	salilab.org/modeller
CGenFF	Mackerell Lab	cgenff.umaryland.edu
GROMACS 2021.4	Science for Life Laboratory	www.gromacs.org
PLUMED 2.9.0-dev	Bonomi et al.	github.com/plumed
MDTraj 1.9.4	McGibbon et al.	mdtraj.org
PyEMMA 2.5.11	CMB Group	www.emma-project.org
Original Code	Filizola Lab	https://doi.org/10.5281/zenodo.7158426

Deposited data

beta2 adrenergic receptor-Gs protein complex	https://www.rcsb.org/structure/3sn6	3SN6
G α_s complexed with GTP γ S	https://www.rcsb.org/structure/1azt	1AZT

(Continued on next page)

Continued

REAGENT or RESOURCE	SOURCE	IDENTIFIER
GDP-bound Gs heterotrimer	https://www.rcsb.org/structure/6eg8	6EG8
nanobody-stabilized active state of the beta2 adrenoceptor	https://www.rcsb.org/structure/3p0g	3P0G
G α s with the catalytic domains of mammalian adenylyl cyclase	https://www.rcsb.org/structure/1azs	1AZS

RESOURCE AVAILABILITY

Lead contact

Further information and requests for resources and reagents should be directed to and will be fulfilled by the lead contact, Ka Young Chung (kychung2@skku.edu).

Materials availability

All unique/stable reagents generated in this study are available from the [lead contact](#) with a completed materials transfer agreement.

Data and code availability

- Data reported in this paper will be shared by the [lead contact](#) upon request.
- All original code has been deposited at Zenodo and is publicly available as of the date of publication. The DOI is listed in the [key resources table](#). Any additional information required to reanalyze the data reported in this paper is available from the [lead contact](#) upon request.

EXPERIMENTAL MODEL AND SUBJECT DETAILS

Human β_2 AR was expressed in Sf9 insect cells infected with BestBac recombinant baculovirus (Expression Systems, Davis, CA, USA). The Gs heterotrimer for HDX-MS was expressed in *Trichoplusia ni* insect cells (Expression Systems). Wild-type or mutant G α s for TrIQ was expressed in the *Escherichia coli* BL21 (DE3) strain, and G α s AHD and MAGE D2 MHD were expressed in *E. coli* LOBSTR strain.

METHOD DETAILS

Expression and purification of the β_2 AR

The full-length β_2 AR was prepared as previously described.²⁷ In brief, recombinant baculovirus was prepared using the Bestbac expression system (Expression Systems) and pVL1392 as a transfer vector. The full-length β_2 AR was expressed by infecting Sf9 cells with second-passage baculovirus stock. The β_2 AR antagonist alprenolol (2 μ M) was added to stabilize the receptor during expression. The infected cells were harvested after 48 h of incubation at 27°C. Cell pellets were lysed, and the receptor was extracted from the cell membrane using a Dounce homogenizer in solubilization buffer [20 mM HEPES, pH 7.5, 100 mM NaCl, 1% dodecylmaltoside (DDM), 1 μ M alprenolol, 2.5 μ g/mL leupeptin, and 160 μ g/mL benzamidine] for 1 h at room temperature (22–25°C). The receptor bearing the N-terminal FLAG tag was then captured by M1 antibody affinity chromatography (Sigma-Aldrich, St. Louis, MO, USA) and further purified by affinity chromatography using alprenolol–Sepharose as previously described⁷⁴ to select functional receptors. The purified receptor with alprenolol was tandem-linked to the M1 FLAG column and washed with HMS–CHS buffer (20 mM HEPES, pH 7.5, 350 mM NaCl, 0.1% DDM, 0.01% cholesterol hemisuccinate) for removal of alprenolol to obtain an unliganded receptor. The receptor was then eluted from the M1 resin with HMS–CHS buffer supplemented with 5 mM EDTA, 200 μ g/mL free FLAG peptide, and 10 μ M BI-167107. Size-exclusion chromatography with a Superdex-200 column (GE Healthcare Life Science, Uppsala, Sweden) equilibrated in HLS–CHS buffer (20 mM HEPES pH 7.5, 150 mM NaCl, 0.1% DDM, 0.01% cholesterol hemisuccinate, 2 μ M BI-167107) was finally used to polish the receptor. BI-167107 is a high-affinity β_2 AR agonist that was used to solve the high-resolution crystal structure of β_2 AR.¹⁸ The receptor was concentrated to 150 μ M for preparing samples for HDX-MS analyses.

Expression and purification of Gs and Gβγ

Heterotrimer Gs and Gβγ were prepared as previously described.²⁷ In brief, for heterotrimeric Gs purification, bovine Gαs (short isoform), His6-rat Gβ1, and bovine Gγ2 were co-expressed in *Trichoplusia ni* insect cells grown in ESF 921 medium (Expression Systems) using two separate *Autographa californica* nuclear polyhedrosis viruses containing the Gαs and Gβγ genes. Cell pellets expressing G protein subunits were resuspended in lysis buffer (10 mM Tris, pH 7.4, 100 μM MgCl₂, 5 mM β-ME, 10 μM GDP, 2.5 μg/mL leupeptin, and 160 μg/mL benzamidine) for 30 min at room temperature (22–25°C). The lysate was spun for 15 min at 18,000 g, and then the pellet was homogenized in solubilization buffer (20 mM HEPES, pH 7.5, 100 mM NaCl, 1% sodium cholate, 0.05% DDM, 5 mM MgCl₂, 2 μL calf intestinal alkaline phosphatase, 5 mM β-ME, 10 μM GDP, 5 mM imidazole, 2.5 μg/mL leupeptin, and 160 μg/mL benzamidine) using a 100-mL Dounce homogenizer and tight pestle. The heterotrimeric Gs was purified using nickel-bound Chelating Sepharose Fast Flow and Q Sepharose resin. The purified protein was passed through a 0.22-μm filter and spin-concentrated in a 10-kDa MWCO concentrator (Millipore, Burlington, MA, USA) to approximately 20 mg/mL. The methods used for the expression and purification of lipidated Gβ1γ2 were very similar to those described for the Gs heterotrimer, except that GDP and MgCl₂ were removed from the buffer formulation.

Expression and purification of Gαs, Gαs AHD, and MAGE D2 MHD

Recombinant Gαs containing an N-terminal His-tag and HRV 3C protease cleavage site was constructed in the pET28a vector. The cDNA of the human MAGE D2 MHD sequence (GenBank: NM_014599; amino acids 261–521) was synthesized and inserted into pET-28a with an N-terminal 6 histidine tag-TEV cleavage site. The cDNA of the human Gαs AHD (GenBank: NM_080426; amino acids 68–206) was synthesized and inserted into pET-28a with an N-terminal 6 histidine tag-thrombin cleavage site and C-terminal FLAG tag. Gαs was transformed into *E. coli* BL21 (DE3), and MAGE D2 MHD and Gαs AHD were transformed into *E. coli* LOBSTR for protein expression. The cells were grown in Terrific Broth in the presence of antibiotic at 37°C until the optical density at 600 nm reached 0.6–0.8. Gαs or MAGE D2 MHD expression was induced by adding 0.5 mM isopropyl β-D-1-thiogalactopyranoside (IPTG) following incubation at 25°C for 18 h or 4 h, respectively. Gαs AHD expression was induced by adding 0.5 mM IPTG following incubation at 37°C for 4 h. For protein purification, the bacterial pellets were suspended in lysis buffer [20 mM HEPES, pH 7.4, 300 mM NaCl, 5 mg/mL lysozyme, 1:1000 protease inhibitor cocktail, 2.5 μg/mL leupeptin, 10 μg/mL benzamidine, 100 μM tris(2-carboxyethyl)phosphine (TCEP)] and incubated for 30 min. The lysates were spun down at 18,000 g for 20 min at 4°C, and the supernatant was collected and loaded onto an Ni-NTA column pre-equilibrated with the lysis buffer supplemented with 20 mM imidazole. The resin was washed with wash buffer (20 mM HEPES, pH 7.4, 100 mM NaCl, 100 μM TCEP, 20 mM imidazole), and the bound proteins were eluted with elution buffer (20 mM HEPES, pH 7.4, 100 mM NaCl, 100 μM TCEP, 200 mM imidazole). The eluted products were loaded onto a Superdex-200 (10/300) column equipped with an ÄKTA FPLC system (GE Healthcare Life Sciences), and the purified proteins were eluted with a second elution buffer (20 mM HEPES, pH 7.4, 100 mM NaCl, 100 μM TCEP). For Gαs, before loading onto the Superdex-200 (10/300) column, the His-tag was removed by incubation with 3C protease at 4°C overnight. Through the purification step, for Gαs purification, 2 mM MgCl₂ and 20 μM GDP were supplemented in the lysis, wash, and elution buffers.

Nucleotide-free β2AR-Gs complex formation

The nucleotide-free β2AR-Gs complex was prepared as previously described.²⁷ In brief, 65 μM of Gs was mixed with 65 μM β2AR at room temperature (22–25°C). Apyrase (200 mU/mL) was added after 90 min of incubation to hydrolyze the GDP released from Gαs, and incubation was proceeded for a further 90 min.

Pulse-labeling HDX-MS

For pulse-labeling deuterium exchange, the β2AR, GDP-bound Gs, and nucleotide-free β2AR-Gs complex were prepared at a concentration of 65 μM. Four microliters of the β2AR or GDP-bound Gs was mixed with 26 μL of D₂O buffer (20 mM HEPES, pH 7.5, 100 mM NaCl, 2 μM agonist, 100 μM TCEP, 0.1% DDM in D₂O) and incubated for 10 s at room temperature (22–25°C). Four microliters of the nucleotide-free β2AR-Gs complex was aliquoted at specific time points (before adding GTPγS and after adding 500 μM GTPγS for 5 s, 30 s, 2 min, 5 min, 10 min, and 30 min) at room temperature (22–25°C) and mixed with 26 μL of D₂O buffer at room temperature (22–25°C). All deuterium-exchanged samples were quenched by 30 μL of ice-cold quench buffer (0.1 M NaH₂PO₄, 20 mM TCEP, pH 2.01), immediately frozen on dry ice, and

stored at -80°C . For non-deuterated samples, 4 μL of protein samples (65 μM) were mixed with 26 μL of H_2O buffer (20 mM HEPES, pH 7.4, 100 mM NaCl, 0.1% DDM in H_2O) to which 30 μL of ice-cold quench buffer was added and snap-frozen on dry ice.

The quenched samples were digested and analyzed by an HDX-ultra-pressure liquid chromatography (UPLC)-electrospray ionization (ESI)-MS system (Waters, Milford, MA, USA) as previously described.²⁷ In brief, quenched samples were thawed and immediately injected into an immobilized pepsin column (2.1 \times 30 mm) (Life Technologies, Carlsbad, CA, USA) at 10°C . Peptide fragments were subsequently collected on a C18 VanGuard trap column (1.7 μm \times 30 mm) (Waters, Milford, MA, USA) for desalting and then isolated by UPLC using an Acquity UPLC C18 column (1.7 μm , 1.0 \times 100 mm) (Waters). To minimize the back-exchange of deuterium to hydrogen, the system, including the trapping column and UPLC column, was maintained at 0.5°C during the analysis, and all buffers were adjusted to pH 2.5. Mass spectral analyses were performed with a Xevo G2 quadruple time-of-flight system equipped with a standard ESI source in MS^{E} mode (Waters) and positive-ion mode. All settings/conditions for the system, such as voltages, temperatures, collision energies, and lockspray, were as previously reported.²⁷ Peptic peptides were identified in non-deuterated samples with ProteinLynx Global Server 2.4 (Waters) with variable methionine oxidation modification, and the peptides were filtered according to a peptide score of 6. To process the HDX-MS data, the amount of deuterium in each peptide was determined by measuring the centroid of the isotopic distribution using the DynamX 2.0 software package (Waters). The average back-exchange level in our system was 30–50%, which was not corrected because the $\beta_2\text{AR}$ only aggregated in the fully deuterated sample condition, and the analyses were based on a comparison of different states of proteins.

Measurement of the separation between the RD and AHD

To measure the separation between the RD and AHD, we used a tryptophan-induced bimane quenching (TriQ) method. First, we mutated residue A303 in the $G_{\alpha s}$ RD, which is adjacent to the AHD, into Cys for monobromobimane labeling. Residue E164 in the $G_{\alpha s}$ AHD was mutated into Trp. The distance between A303 and E164 is 10.7–10.8 \AA in the GDP-bound or $\text{GTP}\gamma\text{S}$ -bound $G_{\alpha s}$ crystal structures (PDB: 6EG8 and PDB: 1AZT, respectively). At this distance, a Trp residue at position 164 would be close enough to quench the fluorescence of the bimane at position 303. In the $\beta_2\text{AR}$ -Gs crystal structure (PDB: 3SN6), these residues are further apart due to displacement of the AHD, and therefore the quenching effect disappears.

Solvent-exposed Cys residues (C174, C200, C237) in $G_{\alpha s}$ were mutated into Ser to prevent unwanted bimane labeling. All mutations were generated by site-directed mutagenesis using polymerase chain reaction (PCR). The engineered $G_{\alpha s}$ was incubated with a 2-molar excess of monobromobimane at room temperature (22 – 25°C) for 1 h. The unbound bimane was removed by buffer exchange with the reaction buffer (20 mM HEPES, pH 7.4, 100 mM NaCl, 2 mM MgCl_2 , 10 μM GDP, 0.1% DDM, 0.01% CHS, 1 μM BI-167107). The bimane-labeled $G_{\alpha s}$ formed a heterotrimer with $\text{G}\beta\gamma$ by incubating at room temperature (22 – 25°C) for 30 min. To form the $\beta_2\text{AR}$ -Gs complex, the heterotrimeric G protein was mixed with the $\beta_2\text{AR}$ for 90 min, followed by another 90 min incubation with Apyrase, which hydrolyzes GDP. The bimane fluorescence was measured by excitation at 390 nm (bandwidth 10 nm) and emission at 485 nm (bandwidth 10 nm) using a BioTek Synergy 2 microplate reader (Santa Clara, CA, USA). $\text{GTP}\gamma\text{S}$ (500 μM) was added, and the bimane fluorescence was measured every 10 s for a total of 2,400 s. All experiments were conducted at room temperature (22 – 25°C).

Nucleotide exchange assay

The nucleotide exchange function of $G_{\alpha s}$ was evaluated by the binding of BODIPY-FL- $\text{GTP}\gamma\text{S}$ (Invitrogen, Waltham, MA, USA) into the GDP-bound $G_{\alpha s}$. BODIPY-FL- $\text{GTP}\gamma\text{S}$ (250 nM) was prepared in an imaging buffer (20 mM Tris pH 8.0, 1 mM EDTA, 10 mM MgCl_2 , 100 μM TCEP). The fluorescence baseline was recorded by TriStar2 S LB 942 Multimode Microplate Reader (Berthold Technologies, Bad Wildbad, Germany) for 120 s. The samples were excited at 485 nm (bandwidth, 14 nm) and detected the emission at 535 nm (bandwidth, 25 nm) in a 96-well black plate. 1.5 μM of GDP-bound $G_{\alpha s}$ was added, and the fluorescence was measured every 10 s for a total of 2,400 s. All experiments were conducted at room temperature (22 – 25°C).

Y2H assay

Y2H screening was conducted by Panbionet (Pohang, South Korea). The AHD (residues 68–192) of GNAS cDNA (375 bp) was amplified by PCR. The PCR product was cloned into a pGBKT7 vector containing the

DNA-binding domain (BD) of GAL4. *Saccharomyces cerevisiae* (yeast) strain PBN240 (Panbionet) was co-transformed with the GAL4 DNA-BD fused to GNAS68–192 and the cDNA activation domain (AD) library. The PBN204 strain contains three reporters (*URA3*, *lacZ*, and *ADE2*) that are under the control of different GAL promoters. The protein–protein interaction was tested using three independent reporters with different types of GAL4-binding sites to reduce the possibility of picking up false-positive candidates; in some cases, reporter gene expression can be activated by an AD fusion protein in a particular GAL promoter-specific manner. Yeast transformants of the GNAS bait and the human kidney cDNA AD library were spread on a selection medium [SD-leucine, tryptophan, uracil (SD-LWU)] that supports the growth of yeasts with bait and prey plasmids, yielding proteins interacting with each other. After selecting yeast colonies on uracil-deficient media, the activity of beta-galactosidase was monitored. The URA⁺ and lacZ⁺ colonies were monitored to see if they were able to grow on adenosine-deficient media. To confirm the interaction, the prey parts of DNA from 60U + A+Z⁺ candidates were amplified by PCR or by *E. coli* transformation, and then the amplified candidate prey was reintroduced into yeast with the GNAS bait plasmid or with a negative control plasmid.

Microscale thermophoresis (MST) assay

The MAGE D2 MHD was fluorescently labeled using Monolith Protein Labeling Kit RED-NHS 2nd Generation (NanoTemper, München, Germany) according to the manufacturer's instructions. Labeled MAGE D2 MHD (50 nM) and two-fold serially diluted *Gαs* AHD (7.629 nM–25 μM) were mixed in the interaction buffer (20 mM HEPES, pH 7.4, 100 mM NaCl, 100 μM TCEP, 0.05% Tween-20). The measurement was conducted with Monolith NT.115 (NanoTemper) at 20% excitation power and medium MST power at 25°C. The results were acquired from MST-on of 5 s.

Immunostaining

cDNAs encoding the AHD open reading frames of *Gαs* cDNA were synthesized according to the GenBank ID NM_080426 and were cloned into the *AsiI* and *PmeI* restriction sites of pCMV6-AC-GFP (Origene, Rockville, MD, USA) using the Gibson assembly (NEB, Ipswich, MA, USA). The 3X FLAG-tag sequence (5'-gac-tacaaagaccatgacgggtgattataaagatcatgacatcgattacaaggatgacgatgacaag-3') was inserted before the stop codon of the *Gαs* AHD. HEK293T cells were seeded 24 h prior to transfection at a density of 2×10^4 cells onto cover glasses in a 24-well plate. pCMV6-*Gαs* AHD-3XFLAG was prepared in Transfection Optimization Media (TOM) and transfected into cells using Lipofectamine 3000. The total amount of plasmids was adjusted to 400 ng. After 24 h, the cells were washed with phosphate-buffered saline (PBS) and fixed for 15 min using 4% of formaldehyde in PBS. Fixed cells were permeabilized for 15 min with 0.1% Triton X-100. Cells were then blocked with 1.5% of bovine serum albumin in PBS for 60 min and labeled with the indicated antibodies overnight. Alexa Fluor-488 and -647 antibodies were used as secondary antibodies. Sixty minutes after treatment with secondary antibodies, the cells were treated with Hoechst 33342 solution (Invitrogen) for 20 min. After the last wash, the cells were dried and mounted with mounting solution.

Immunoprecipitation and immunoblot analysis

HEK293T cells were seeded 24 h prior to transfection at a density of 5×10^6 cells in 100-mm dishes. pCMV6-MAGE D2-turboGFP and pCMV6-*Gαs* AHD-3XFLAG were prepared in TOM and transfected into cells using Lipofectamine 3000. The total amount of plasmids was adjusted at 1000 ng. After 24 h, the cells were washed with PBS and lysed with RIPA buffer in the presence of a protease inhibitor cocktail. SureBeads Protein G magnetic beads (Bio-Rad, Hercules, CA, USA) and anti-FLAG (1:1000) were added to the transferred lysates and incubated overnight. Proteins bound to antibodies and protein G Sepharose were collected by centrifugation and washed three times with RIPA buffer. The precipitated samples were boiled in SDS-PAGE sample loading buffer (Abpbio, Beltsville, MD, USA) for 10 min at 95°C. Proteins and a molecular-weight marker (Bio-Rad) were subjected to Tris-glycine SDS-PAGE and then transferred onto polyvinylidene fluoride membranes. The membrane was blocked with 5% skim milk in TBS-T buffer, incubated with the primary antibody at 4°C overnight, and then incubated with horseradish peroxidase-conjugated secondary antibody for 60 min at room temperature (22–25°C). Immunoblots were visualized using AbSignal western blotting detection reagent (AbClon, Seoul, Republic of Korea) and detected using Bio-Rad ChemiDoc (Bio-Rad).

Systems setup for simulations

The crystal structure of the activated bovine $G\alpha_s$ bound to $GTP\gamma S$ and Mg^{2+} (PDB ID: 1AZT²²) was used as a reference conformation of the protein with a closed AHD. All non-protein atoms except for the Mg^{2+} ion and $GTP\gamma S$ were removed. Missing residues 9–34 and 392–394 were modeled based on the crystal structure of human Gs in complex with GDP (PDB ID: 6EG8;²⁰), using the “Protein Splicing” tool within the Schrödinger’s Maestro software package.⁷⁵ Residues 70–73, which were missing from both crystal structures, were added using the “Crosslink Proteins” panel in Maestro, and their conformation was predicted using the “Loop lookup” option to search for known geometries in the PDB. The nucleotide-free form of $G\alpha_s$ bound to $G\beta\gamma$ subunits and the agonist BI167107-bound β_2AR (PDB: 3SN6¹⁸) were also prepared using standard protocols of the Maestro software package,⁷⁵ with engineered residues in the 3SN6 construct converted into wild-type human residues. Missing short segments in β_2AR (176–178) or $G\alpha_s$ (53–64, 70–87, and 256–262) were built either with MODELLER 9.19^{76,77} based on available templates (PDBs: 3P0G,¹⁸ 1AZS,⁶⁵ 6EG8,²⁰ and 1AZT,²² respectively) or *ab initio* ($G\alpha_s$ 65–69 and 203–204), whereas longer missing segments or termini (β_2AR 1–29, 240–264, and 342–413, as well as $G\alpha_s$ 1–8 and $G\gamma$ 1–4 and 63–71) were not modeled and their ends were capped. These segments, which correspond to the very flexible N-terminal (1–29), intracellular loop 3 (240–264) and C-terminal regions (342–413) of β_2AR , the N-terminal region of $G\alpha_s$ (1–8), and the N-/C-terminal regions of $G\gamma$ (1–4 and 63–71), are all far from the G protein region (i.e., AHD-RD interface) that is sampled during simulations (see below) and are therefore assumed to have no effect on its dynamic behavior.

Molecular dynamics simulations for energy minimization and equilibration

After adding hydrogens and Mg^{2+} in the nucleotide binding pocket, the aforementioned $GTP\gamma S$ -bound $G\alpha_s$ system with $GTP\gamma S$ modeled using the CHARMM general force field (CGenFF)⁷⁸ was immersed in a dodecahedron water box of TIP3P water molecules⁷⁹ in such a way that there were at least 10 Å of water molecules between the protein and the boundary of the unit cell in all directions. The nucleotide-free β_2AR -Gs system with CGenFF-derived parameters for the β_2AR ligand BI-167107 was embedded in a POPC/10% cholesterol membrane patch and solvated in TIP3P water to form a $122 \times 122 \times 170 \text{ \AA}^3$ simulation box. The NaCl concentration was set to 0.15 M, and the proteins were modeled using the CHARMM36m⁸⁰ force field, with a 12 Å cutoff set for non-bonded interactions. We used the non-bonded interaction FIX corrections to the CHARMM36 force-field, which provide an improved parameterization of Mg^{2+} ions for biomolecular systems as reported in the literature.⁸¹ Long-range electrostatic interactions were calculated using the particle-mesh Ewald method.⁸² All bonds containing hydrogen atoms were fixed using the LINCS algorithm,⁸³ while hydrogen masses were increased to 4 amu using the mass repartition scheme,⁸⁴ so that production molecular dynamics simulations could be executed with a time step of 4 fs. Both $GTP\gamma S$ -bound $G\alpha_s$ and nucleotide-free β_2AR -Gs systems were minimized and subsequently equilibrated to a temperature of 300 K using the Nose-Hoover thermostat^{85,86} and to a pressure of 1 atm using the Parinello-Rahman barostat^{87,88} by unrestrained molecular dynamics simulations using the Gromacs 2021.4 software package.⁸⁹ After gaining experience simulating the monomeric $GTP\gamma S$ -bound state of $G\alpha$ for 50 ns, we carried out simulations of the larger system with $G\alpha$ bound to both the receptor and $\beta\gamma$ subunits, checking for convergence more frequently, and eventually stopping the equilibration run at 10 ns. Figures S4A–S4C show evidence that the solvent and lipid bilayer are sufficiently equilibrated in both systems after only 10 ns. The radial distribution function (RDF) for the phosphorus atoms in each leaflet is stable after the first half of the equilibration run (Figure S4A), with the first peak at 6.25 Å, which corresponds to an area-per-lipid of 67.7 Å²/lipid, in agreement with experimental values for POPC.⁹⁰ The RDF for water is also stable after the first half of the equilibration (Figure S4B) and follows the characteristic profile of the TIP3 model.⁹¹ The stability of the various protein domains during equilibration is shown in shown in Figure S4C.

Metadynamics simulations for exhaustive conformational sampling

The conformational rearrangement between the closed and open states of the $G\alpha_s$ AHD in both $GTP\gamma S$ -bound $G\alpha_s$ and nucleotide-free β_2AR -Gs systems was simulated using well-tempered metadynamics simulations^{35,92,93} to enhance sampling along two collective variables. Specifically, CV1 corresponded to a plane projection of the angle between the two vectors connecting the $C\alpha$ atoms of the AHD residues 95 and 106 or the RD residues 58 and 341 of the $G\alpha_s$ subunits, whereas CV2 accounted for the deviation of the contact map between the two domains with respect to one derived from PDB: 1AZT. This deviation was measured by monitoring the distances between the $C\alpha$ atoms of all pairs of residues on the two domains that are within 8 Å of each other in the starting (closed) structure of 1AZT. Smooth switching

between contacts being formed and broken was accomplished using a rational switching function $(1 - (r/r_0)^6)/(1 - (r/r_0)^{12})$, where r is the distance between the $C\alpha$ atoms of the interacting residues and r_0 was set to 8.0 Å. Well-tempered metadynamics simulations were performed with Gromacs 2021.4 interfaced with the PLUMED library,^{94,95} adding Gaussian hills every 1000 steps with an initial height of 1.0 kJ/mol and a bias factor of 10, and with a width of 0.05 rad and 0.1 for the angle and contact dimensions, respectively. Reweighting factors to recover unbiased values from the simulations were calculated using an established methodology.⁹⁶ Simulations were carried out at a temperature of 300 K and pressure of 1 atm with a time step of 4 fs, as described above for the unbiased simulations. Data were recorded every 20 ps. The total metadynamics simulation time was 7.6 μ s and 7.0 μ s for the GTP γ S-bound G α s and nucleotide-free β_2 AR-Gs systems, respectively. Convergence was assessed by plotting changes in free energy as a function of the two aforementioned CVs, using first-quarter, half, three-quarters, and the whole trajectories (Figure S5B). Evidence that the initial models of the missing loops are simulated for a sufficient amount of time for them to explore the conformations of different functional states is provided in Figure S5C, where the RMSD evolution of the linker-1 (14 residues, M60-E87) and switch III (6 residues, V256-A262) loops during metadynamics simulations is presented as an example.

Clustering of metadynamics-derived conformational states

To identify the different conformations sampled by the GTP γ S-bound G α s and nucleotide-free β_2 AR-Gs systems during metadynamics simulations, the resulting trajectories were clustered using the pairwise distances between every third $C\alpha$ atom in G α s (6,441 distance pairs). Residues 9–32 of the α N helical domain and residues 33–38 of the α N/ β 1 loop were left out from this analysis because they were very flexible during simulations of GTP γ S-bound G α s, which was assumed to be due to the absence of G $\beta\gamma$. The pairwise distances were calculated using batches of 20 frames from each trajectory (18,910 and 17,601 frames for the GTP γ S-bound G α s and nucleotide-free β_2 AR-Gs systems, respectively), and their values were projected onto the first 10 time-structure independent component analysis (tICA) components. Pooled tICA features from the two systems were partitioned in 10 groups using k-means clustering, and each cluster was split into two, resulting in a total of 20 clusters. Four of these 20 clusters were empty as they were derived from splitting into two clusters conformations in which the AHD assumed specific conformational states in one simulated system but not the other, resulting in a total of 16 populated clusters. Of these 16 clusters, R_s , nine pertained to the GTP γ S-bound G α s system and seven to the nucleotide-free β_2 AR-Gs system. The structural homogeneity of these clusters is shown in Figure S7A. Although hyperparameters were not systematically explored to identify an optimal clustering, the results from 5 to 10 initial clusters were compared and the 10 clusters ultimately chosen because the final model conveyed better agreement with experimental data. Finally, 10 frames from each cluster were sampled as representatives, which were used to calculate the values of the protection factors $\langle PF \rangle_s$ and deuterium uptake $D_J(s)$ as input for the kinetic modeling described below. Calculation of the RMSD values, as well as the atom–atom distances needed for the estimation of the protection factors (see below), was carried out with MDTraj,⁹⁷ whereas the tICA and clustering analyses were performed with PyEMMA.⁹⁸

Prediction of protection factors from metadynamics-sampled conformations

HDX experiments probe the rate of exchange of backbone amide hydrogens with deuterium (2 H or D) upon solvation into D_2O . The hydrogen/deuterium exchange rate of a specific residue is affected by the macroscopic environment (e.g., pressure, temperature, ionic strength of the solvent), as well as the nature of the amino acids immediately preceding and following the residue in the protein sequence,^{99,100} long-range electrostatic interactions,¹⁰¹ and local distribution of charged residues.¹⁰² In particular, the involvement of backbone amide hydrogens in hydrogen bonding with buried residues of a protein can slow down this exchange. This slowdown is commonly expressed in terms of protection factors $P = k_{\text{obs}}/k_{\text{int}}$, where k_{obs} is the observed exchange rate and k_{int} is the “intrinsic” exchange rate in the fully unprotected, solvent-accessible state. Values of k_{int} for each residue in a protein are typically not available and are instead approximated by the values measured for short peptides flanked by poly-D/L-alanine. In this work, we adopted intrinsic rates⁹⁹ of the following form:

$$k_{\text{int}} = k_A^{\text{Ref}}(A_L A_R)[D^+] + k_B^{\text{Ref}}(B_L B_R)[OH^-] + k_w^{\text{Ref}}(B_L B_R) \quad (\text{Equation 1})$$

where $[D^+]$ and $[OH^-]$ are the deuteron and hydroxide concentrations, respectively; k_A^{Ref} , k_B^{Ref} , and k_w^{Ref} are values for side chain-specific acid, base, and water rate constants, respectively; and A_L , A_R , B_L , and B_R are correction factors that depend on the residue on the left and right side of the reference residue, respectively.

A semi-empirical approximation of protection factors of a protein in a given conformation R introduced by Vendruscolo et al.,¹⁰³ and later generalized by Wan et al.,¹⁰⁴ expresses the protection factors for the protein in a conformational ensemble R_s as:

$$\log PF_{sim}(R_s) = \langle \beta_C N_C(R) + \beta_H N_H(R) + \beta_0 \rangle_{R_s} \quad (\text{Equation 2})$$

Where $N_C(R)$ is the number of heavy atoms within a given cut-off distance d_C from the amide nitrogen, $N_H(R)$ is the number of hydrogen bonds formed by the amide, the β s are model coefficients, and the average is calculated overall conformations R in the ensemble R_s . To calculate, using Equation 2, the protection factors in the clusters R_s identified for our systems, we defined N_C and N_H using sigmoid switching functions:

$$N_i(R) = \sum_j \frac{e^{-b(x_{ij}-d)}}{1 + e^{-b(x_{ij}-d)}} \quad (\text{Equation 3})$$

where x_{ij} is the distance between the amide on residue i and atom j in conformation R , and b and d are parameters that determine the effective cut-off distance used to derive the values of N_C and N_H . The sum is extended to all heavy atoms j for the calculation of N_C , and to all hydrogen bond acceptors for the calculation of N_H . The original application¹⁰³ used $\beta_0 = 0$, and the coefficients β_C and β_H were obtained by the least-squares fit of Equation 2 to the HDX experimental results obtained for the native state of seven different globular proteins, and fixed to $\beta_C \approx 0.35$ and $\beta_H \approx 2$. The values of the distance cutoffs were fixed to $d_C = 6.5 \text{ \AA}$, and a cutoff of $d_H = 2.4 \text{ \AA}$ between hydrogen donors and acceptors was used to identify hydrogen bonds.¹⁰³

Bayesian inference was used to determine the parameters $\{\beta_C, \beta_H, \beta_0, b, d_C, d_H\} = \theta$ of the model as proposed by Wan et al.¹⁰⁴ Specifically, the joint distribution of the parameters was expressed as:

$$p(\theta, \sigma | O) = p(O | \theta, \sigma) p(\theta, \sigma) \quad (\text{Equation 4})$$

where $p(O | \theta, \sigma)$ is the likelihood of the observed data O derived from Equation 2 with a Gaussian error structure of variance σ^2 :

$$\log p(O | \theta, \sigma) = -\frac{1}{2} \log 2\pi\sigma^2 - \sum_i \frac{(\log PF_{sim}(R) - \log PF_{exp}(R))^2}{2\sigma^2} \quad (\text{Equation 5})$$

The full posterior $p(\theta, \sigma | O)$ in the original implementation was sampled using experimental data available on two globular proteins.¹⁰³ In this work, we adopted the distribution sampled in Wan et al.¹⁰⁴ as the prior distribution for HDX modeling.

Prediction of quenching data using metadynamics-sampled conformations

The separation and relative orientation between the Gas RD and AHD were probed experimentally by measuring the quenching of the emission intensity of bimane, an organic fluorophore, by electron-donating residues (e.g., tryptophan and tyrosine) or moieties (e.g., guanine), using photoinduced electron transfer (PET).^{105–107} Unlike Förster resonance energy transfer, which typically monitors longer distances, PET measures quenched fluorescence upon van der Waals contact, thus providing a better estimate of molecular contacts.⁴⁵ Given a conformational ensemble characterized by the probability distribution $\mu(R)$, we express the bimane fluorescence intensity as:

$$F_i = F_0 \int \mu(R) \vartheta(U_j\{d_{b,j} - d_{0,j}\}) \approx F_0 p(U_j\{d_{b,j} - d_{0,j}\}) \quad (\text{Equation 6})$$

where F_i is the measured quenched fluorescence, F_0 is the bimane intensity in the absence of quenching, $d_{b,j}$ is the distance between the bimane and electron-donating moiety j , $d_{0,j}$ is the appropriate distance cutoff for the quenching moiety, and $U_j\{d_{b,j} - d_{0,j}\}$ represents the case wherein at least one quencher moiety is close enough to the fluorophore. Adopting previously published reference values,¹⁰⁷ we used 15 Å as an appropriate distance cutoff for quenching induced by tryptophan and 10 Å for quenching induced by tyrosine.

Bayesian inference to update metadynamics-derived prior probabilities of conformational states with pulsed HDX-MS and fluorescence quenching data

Pulsed HDX-MS probes the time-dependence of the total deuterium uptake by a protein exposed to D₂O for short pulses of time. The fraction of deuterated amino acids $D_J(s)$ for a peptide segment J of the protein

in each conformational ensemble s can be calculated for a pulse τ using the protection factors of the individual residues $j \in J$ of the peptide as:

$$D_J(s) = \frac{1}{n_J} \sum_{j \in J} \left(1 - \exp\left(-\frac{\tau k_{\text{int}}^{(j)}}{\langle PF_j \rangle_s}\right) \right) \quad (\text{Equation 7})$$

where $\langle PF_j \rangle_s$ is the average protection factor for residue j in state s and $k_{\text{int}}^{(j)}$ is the intrinsic rate for residue j . We assume that the state of the system can be described as a Markov process between conformational states s , with a transition rate matrix \mathbf{k} , so that the transition probabilities from one metadynamics-derived cluster to another can be expressed as $\exp(\mathbf{k}t)$. Given this model, the probability that the system is in each state at time t can be expressed as $\boldsymbol{\pi}(t) = \boldsymbol{\pi}(0) \exp(\mathbf{k}t)$, where $\boldsymbol{\pi}(0)$ is the initial probability distribution and \mathbf{k} is the transition matrix describing the kinetics of the protein. Using these probabilities, the time-dependence of the observed D_J values can be expressed as:

$$D_J(t, \mathbf{k}, \boldsymbol{\pi}(0), \theta) = \sum_s \pi_s(t) D_J(s) = \sum_{sr} \pi_r(0) (e^{t\mathbf{K}})_{sr} D_J(s) \quad (\text{Equation 8})$$

where θ is the parameter that determines the values of $D_J(s)$ in Equation 7. The log-likelihood of the observed HDX data for a given value of the model parameters $(\mathbf{k}, \boldsymbol{\pi}(0), \theta)$ is

$$\log p(O_{\text{HDX}} | \mathbf{k}, \boldsymbol{\pi}(0), \theta, \sigma_{\text{HDX}}) = -\frac{1}{2} \log 2\pi\sigma_{\text{HDX}}^2 - \sum_{J,t} \frac{(\log D_{J,t}^{\text{sim}} - \log D_{J,t}^{\text{exp}})^2}{2\sigma_{\text{HDX}}^2} \quad (\text{Equation 9})$$

where $D_{J,t}^{\text{sim}}$ is the deuterated fraction for peptide segment J of the protein given by Equation 8, $D_{J,t}^{\text{exp}}$ is the corresponding experimental value, and σ_{HDX} quantifies the uncertainty of experimental measures. The results presented in this analysis were obtained using data for 13 of the peptides reported in Figures 1 and 2 (46–59, p-loop- α 1; 108–118, C-terminus of α A through the α A/ α B loop; 119–126, α A/ α B loop- α B; 126–132, α B; 178–193, α E- α E/ α F loop; 190–197, α E/ α F loop- α F; 201–208, Switch I; 256–272, Switch III- α 3; 290–297, β 5- α G; 297–312, α G- α G/ α 4 loop; 367–371, β 6/ α 5-N-terminus of α 5; 372–381, N-terminal half of α 5; and 382–390, C-terminal half of α 5).

Similarly, we included the values of the bimane fluorescence quenching in the model inference at the beginning of the experiment and at equilibrium. Following the same approach outlined above for HDX, the ratio of the quenched over non-quenched fluorescence is expressed as the probability that at least one quencher moiety is close enough to the fluorophore

$$\varphi_t^{\text{sim}} = \sum_s \pi_s(t) p_t(\cup_j \{d_{b,j} - d_{0,j}\}) \quad (\text{Equation 10})$$

and the likelihood of the observed bimane data is then

$$\log p(O_{\text{FQ}} | \boldsymbol{\pi}(0), \boldsymbol{\pi}) = -\frac{1}{2} \log 2\pi\sigma_{\text{FQ}}^2 - \sum_t \frac{(\log \varphi_t^{\text{sim}} - \log \varphi_t^{\text{exp}})^2}{2\sigma_{\text{FQ}}^2} \quad (\text{Equation 11})$$

Finally, the posterior joint distribution of the parameters that describe the model can be expressed as:

$$p(\mathbf{k}, \boldsymbol{\pi}(0), \theta, \sigma | O) = p(O_{\text{HDX}}, O_{\text{FQ}} | \mathbf{k}, \boldsymbol{\pi}(0), \theta, \sigma_{\text{HDX}}) p(\theta, \sigma) p(\mathbf{k}) p(\boldsymbol{\pi}(0)) \quad (\text{Equation 12})$$

Maximum Caliber priors and sampling to derive the transition matrix

To use Equation 12 to determine the transition matrix, the prior distributions $p(\theta, \sigma)$, $p(\mathbf{k})$, and $p(\boldsymbol{\pi}(0))$ must first be specified. We used the distributions from Wan et al.¹⁰⁴ for the model parameters. In line with the experimental setup, we assumed that the prior distribution for the initial probabilities $p(\boldsymbol{\pi}(0))$ is concentrated on states from the nucleotide-free β_2 AR-Gs system. Thus, we used an informative distribution for $\boldsymbol{\pi}(0)$ by assigning a vanishing probability to the GTP γ S-bound G α s states. We incorporated the maximum entropy (Maximum Caliber) principle¹⁰⁸ into the Bayesian inference by deriving entropic priors $p(\mathbf{k})$ for the kinetic matrix. Following Caticha and Preuss,¹⁰⁹ we express the prior for \mathbf{k} as,

$$p(\mathbf{k}) = \frac{\mu(\mathbf{k}) \exp(S_\ell(\mathbf{k}))}{Z} \quad (\text{Equation 13})$$

where $Z = \int \mu(\mathbf{k}) e^{S_\ell(\mathbf{k})}$ is a normalization factor and $S_\ell(\mathbf{k})$ is the local relative entropy as a function of the transition matrix $\mathbf{k} \in K$

$$S_\ell(\mathbf{k}) = - \int dx p(x|\mathbf{k}) \log \frac{p(x|\mathbf{k})}{m(x)} \quad (\text{Equation 14})$$

To fix the prefactor $\mu(\mathbf{k})$ in Equation 13, we set $(\mathbf{k}) = \sqrt{g}$, where $g = \det g_{ij}$ is the determinant of the information metric induced by $S_\ell(\mathbf{k})$ on the space K :

$$g_{ij} = - \frac{\partial^2 S_\ell(\mathbf{k})}{\partial k_i \partial k_j} \quad (\text{Equation 15})$$

Specifically, if x is the space of Markov paths on a discrete set of microstates and $\mathbf{k} = \{k_{\alpha\beta}\}$ are the rates of transition between the microstates, then the local entropy $S_\ell(\mathbf{k})$ can be written as:

$$S_\ell(\mathbf{k}) = - \sum_{\alpha\beta} \pi_\alpha k_{\alpha\beta} \log k_{\alpha\beta} \quad (\text{Equation 16})$$

It is convenient to fix the stationary probability π_α and work in the subspace of K_π with that distribution, so that

$$g_{\alpha\beta, \alpha'\beta'} = \frac{\partial^2}{\partial k_{\alpha\beta} \partial k_{\alpha'\beta'}} \sum_{\rho\sigma} \pi_\rho k_{\rho\sigma} \log k_{\rho\sigma} = \delta_{\alpha\beta, \alpha'\beta'} \frac{\pi_\alpha}{k_{\alpha\beta}} \quad (\text{Equation 17})$$

The prior distribution for the transition matrix $p(\mathbf{k}|\boldsymbol{\pi})$ is therefore

$$p(\mathbf{k}|\boldsymbol{\pi}) = \frac{e^{S_\ell(\mathbf{k})} \sqrt{g}}{Z} = Z^{-1} \exp\left(- \sum_{\alpha\beta} \pi_\alpha k_{\alpha\beta} \log k_{\alpha\beta}\right) \prod_{\alpha\beta} \left(\frac{\pi_\alpha}{k_{\alpha\beta}}\right)^{\frac{1}{2}} \quad (\text{Equation 18})$$

Given that the experimental conditions are such that GTP γ S saturates G α s at equilibrium, we assumed that the prior distribution for the equilibrium probabilities $p(\boldsymbol{\pi})$ is concentrated on states from the GTP γ S-bound G α s simulation and assigned vanishing probabilities to the states sampled by the nucleotide-free β_2 AR-Gs system.

Using this prior and the likelihoods in Equations 9 and 11, we sampled the full posterior distribution $p(\mathbf{k}, \boldsymbol{\pi}(0), \theta, \sigma|O)$ using a Gibbs sampling algorithm implemented in an in-house Python script. Values of $D_j(t)$ and $\boldsymbol{\pi}(t)$ sampled from the posterior distribution (Equation 12) are reported in Figures S6 and S7B, respectively. Predicted populations of the initial state of the systems (at time 0) were obtained from the sampled marginal posteriors of the initial probabilities, the equilibrium distribution of the states (at long time scales) was obtained from Perron eigenvectors of the sampled transition matrices, and the state probabilities at intermediate times (Figure S7B) were obtained by direct application of the transition matrix.

QUANTIFICATION AND STATISTICAL ANALYSIS

For HDX-MS analysis, the significance of mass differences greater than 0.3 Da between individual time points was tested using a paired *t*-test run in GraphPad Prism software. Comparisons with p-value less than 0.05 were considered statistically significant. &, the HDX level of the nucleotide-free β_2 AR-Gs complex showed a statistically significant difference from the HDX levels of GDP-bound Gs or β_2 AR alone. *, the first time point after GTP γ S addition when the HDX level returned to the HDX levels of the GDP-bound Gs or β_2 AR alone. #, the first time point after GTP γ S addition when the HDX level showed a statistically significant difference from the HDX level of the nucleotidefree β_2 AR-Gs complex but not yet returned to the HDX levels of GDP-bound Gs or β_2 AR alone. +, the first time point showing a statistically significant difference from the time point (*). Error bars indicate the standard error of the mean of three technically independent experiments. Data are displayed using a non-linear/non-logarithmic scale. All of the statistical details are described in figure legends. Results of the kinetic modeling are reported with the average and credible intervals corresponding to the 25% and 75% quantiles of 5,000 samples from the marginal posterior distributions (in Figures S5 and S8 and in Tables S1 and S2).